



MACQUARIE
University
SYDNEY · AUSTRALIA

School of Engineering

Mesoporous Carbon Nitride Based Nanomaterials for Solar Fuel Production

By:

Amanj Kheradmand

Supervisor:

Doctor Yijiao Jiang

November 2018

A thesis submitted in fulfillment of the requirements for the degree in Master of Research

STATEMENT OF CANDIDATE

I, Amanj Kheradmand, declare that this submission is my own work and contains no material formerly published by any other person except where due acknowledgement has been made.

Student's Name: Amanj Kheradmand

Student's Signature: Amanj Kheradmand

Date: 09/11/2018

Acknowledgments

First and foremost, I would like to thank Dr. Yijiao Jiang for her encouragement, guidance and patience throughout this project. Also, I want to thank my colleague, Ms Yuxiang Zhu, who helped me during my experiments. I give my gratitude to Mr Aleksei Marianov for his help and assistance about different aspects of my project. Also, I would like to acknowledge my gratitude to all members of Yijiao's research group. I thank the Microscopy Unit at Macquarie University for TEM characterisation.

Dedication

I dedicate my thesis to my beloved parents for all their love, care, and support throughout my life.
Thank you **Maman** and **Kake** for being with me in every step of my life.

Abstract

From economic and environmental aspects, the generation of hydrogen (H_2) from renewable solar energy and water through photocatalytic water splitting is a promising route, but the development of an efficient catalyst remains a great challenge for its technological use on a large scale. Because of several features like being metal-free, nontoxic, low cost, and chemically stable, carbon nitride has attracted worldwide attention. Compared to bulk carbon nitride, mesoporous carbon nitride (MCN) possesses a higher surface area and plentiful accessible mesopores. For the first time, Co_3O_4 /MCN nanocomposites were designed and synthesised for photocatalytic H_2 evolution in this work. Co_3O_4 , earth-abundant nanoparticles, were supported on MCN via an impregnation method. Complementary characterisation techniques were employed to understand the properties of the fabricated catalysts. The bare MCN prepared under optimum conditions showed high photocatalytic activity under visible light irradiation without using any co-catalyst. The Co_3O_4 /MCN with a Co_3O_4 mass content of 5 wt% exhibited the optimum photocatalytic activity in H_2 evolution, which was two times higher than that of the bare MCN. The improved photocatalytic performance may be attributed to the enhanced catalytic properties, visible-light harvesting and effective charge separation.

Table of Contents

List of figures	vii
List of tables	ix
Chapter 1: Introduction	1
1.1. Background.....	1
1.2. The scope of the thesis.....	2
1.3. The structure of the thesis	2
Chapter 2: Literature Review	3
2.1. Mechanism of photocatalytic H ₂ generation.....	3
2.2. Semiconductor materials for photocatalytic water splitting.....	5
2.2.1. TiO ₂ -based semiconductors	5
2.2.2. Other metal-oxide semiconductors	6
2.2.3. Metal-free materials	7
2.3. Mesoporous carbon nitride (MCN).....	10
2.3.1. Synthesis of MCN.....	10
2.3.1.1. Hard-templating method.....	10
2.3.1.2. Soft-templating method.....	16
2.3.2. Surface modification of MCN.....	17
2.3.2.1. Surface modification by noble metal nanoparticles.....	17
2.3.2.2. Surface modification by non-noble metal nanoparticles.....	20
Chapter 3: Experimental Section	25
3.1. Materials and chemicals.....	25
3.2. Catalyst preparation.....	25
3.2.1. MCN fabrication.....	25
3.2.2. Co ₃ O ₄ fabrication.....	25
3.2.3. Co ₃ O ₄ /MCN fabrication.....	26
3.3 Characterisation	26
3.4 Evaluation of photocatalytic H ₂ production	27
3.5 Electrochemical measurement	27
Chapter 4: Results and Discussion.....	28
4.1. Photocatalytic H ₂ production.....	28
4.1.1. Effect of the ratio of silica template to the precursor.....	28

4.1.2. Effect of the Co_3O_4 content on $\text{Co}_3\text{O}_4/\text{MCN}$	28
4.2. Material characterisation.....	29
4.2.1. XRD.....	29
4.2.2. FT-IR.....	31
4.2.3. BET.....	32
4.2.4. TEM and EDX.....	35
4.2.5. UV-vis diffuse reflectance spectra	36
4.2.6. Photoluminescence.....	37
4.2.7. Transient photocurrent responses.....	38
4.2.8. Mott-Schottky	39
4.2.9. Electrochemical impedance spectroscopy	40
4.3. Photocatalytic mechanism.....	41
Chapter 5: Conclusions and Future Work	45
5.1. Concluding comments	45
5.2. Future work.....	46
References:	47

List of figures

Figure 2-1 Schematic illustration of water splitting over semiconductor photocatalyst.	3
Figure 2-2. Band levels of various semiconductor photocatalysts.	4
Figure 2-3. (a) Reaction pathways for the formation of g-C ₃ N ₄ using cyanamide, (b) Scheme of triazine-based connection in g-C ₃ N ₄	8
Figure 2-4. The band energies of g-C ₃ N ₄ and TiO ₂ , a relative to the redox reactions of water and photoemission energies.	9
Figure 2-5. Scheme of two major routes for the synthesis of MCN: (a) soft-templating and (b) hard-templating method.	10
Figure 2-6. Overall scheme for the synthesis, functionalisation, and applications of the MCN.....	11
Figure 2-7. Synthetic pathways to MCN through hard-templating methods.	12
Figure 2-8. H ₂ -evolution by CN-SBA-16-T samples as a function of reaction time.	13
Figure 2-9. Catalytic performance of MCN prepared by using various dispersing solvents for MCN fabrication.	15
Figure 2-10. The rate of H ₂ evolution on MCN prepared with different mass ratio of P123 to melamine under visible-light irradiation.	17
Figure 2-11. a) FE-HRSEM, b) HRTEM images of Au nanoparticle encapsulated MCN and c) HRSEM image of Au nanoparticle encapsulated AC.....	18
Figure 2-12. (a) STEM, (b) HRTEM, and (c) TEM images of Pd/MCN.....	19
Figure 2-13. (a) Photoluminescence spectra, (b) Photocurrent measurements, (c) UV-vis diffuse reflectance spectra of g-C ₃ N ₄ , mpg-C ₃ N ₄ and 1.5 % Co ₃ O ₄ /mpg-C ₃ N ₄	20
Figure 2-14. Graphic design for preparation of SnCoS ₄ /MCN.	21
Figure 2-15. Formation mechanism of mpgCNS.	22
Figure 2-16. Schematic diagram of the photocatalytic mechanism in WO ₃ /MCN.....	23
Figure 4-1. H ₂ generation of MCN at different ratios of the silica template to the precursor. Reaction condition: 40 mg of catalyst in 40 mL of water/TEA solution (9:1 v/v) under visible light (≥420 nm)	28
Figure 4-2. H ₂ generation of MCN and Co ₃ O ₄ /MCN at different contents of Co ₃ O ₄ . Reaction condition: 40 mg of catalyst in 40 mL of water/TEA solution (9:1 v/v) under visible light (≥420 nm)	29
Figure 4-3. Wide-angle XRD patterns of MCN and Co ₃ O ₄ /MCN with different contents of Co ₃ O ₄	30
Figure 4-4. Low-angle XRD pattern of MCN.	31
Figure 4-5. FTIR spectra of MCN and Co ₃ O ₄ /MCN at different contents of Co ₃ O ₄	32
Figure 4-6. a) Nitrogen adsorption–desorption isotherms, b) Pore size distribution of MCN at different ratios of the silica template to the precursor	33
Figure 4-7. a) Nitrogen adsorption–desorption isotherms, b) Pore size distribution of MCN and Co ₃ O ₄ /MCN at different contents of Co ₃ O ₄	34
Figure 4-8. TEM images of silica template (a), MCN (b) and 5-Co ₃ O ₄ /MCN (c) samples.....	35
Figure 4-9. Energy dispersive X-ray (EDX) analysis and corresponding elemental mapping of N, C, O and Co elements in (a) MCN and (b) 5-Co ₃ O ₄ /MCN.....	36
Figure 4-10. a) UV–vis diffuse reflectance spectra, b) Tauc plots of Co ₃ O ₄ , MCN and 5-Co ₃ O ₄ /MCN.....	37
Figure 4-11. PL spectra of the MCN and 5-Co ₃ O ₄ /MCN.....	38
Figure 4-12. Photocurrent responses under visible-light irradiation with 60 s light on-off cycles of the Co ₃ O ₄ , MCN and 5-Co ₃ O ₄ /MCN.....	39
Figure 4-13. Mott-Schottky plots of a) MCN and b) Co ₃ O ₄	40

Figure 4-14. EIS of MCN and 5-Co ₃ O ₄ /MCN both in dark and under light.	41
Figure 4-15. Schematic band structures of MCN and Co ₃ O ₄ obtaining from Mott-Schottky and electronegativity analysis	43
Figure 4.16 Schematic illustration of the photocatalytic mechanism.	44

List of tables

Table 4-1. Textural properties of MCN samples at different ratios of the silica template to the precursor	33
Table 4-2. Textural properties of MCN samples and Co_3O_4 /MCN at different contents of Co_3O_4	34
Table 4-3. The absolute electronegativity, band gap energy, valence, and conduction band edges of MCN and Co_3O_4 based on a theoretical formula	42

Chapter 1: Introduction

1.1. Background

Meeting the future energy demand, in a way which is to be both safe and abundant, is the greatest challenge of the 21st century. Nowadays, most of our energy resources (almost 80 %) come from fossil fuel¹. On the other hand, these resources will deplete in the future. Also, combustion of fossil fuel emits greenhouse gases which lead to global climate change. Awareness of pollution problems has tremendously increased. The global energy consumption rate in 2013 was 17 terawatts, and it is predicted to nearly double by 2050², and the world's population is increasing every day. As a result, finding clean and renewable energy is required. Having clean energy has various advantages such as economic, social and environmental ones. Among different kinds of energy, solar energy has received great attention, though using solar energy has several drawbacks such as low density and expensive storage cost. An alternative source of energy which is clean, storable, and renewable is needed.

An important clean fuel that has gained much attention during recent decades is hydrogen (H₂). H₂ is the simplest and most common element in the universe. H₂ is an ideal clean fuel of the future because of (1) its ability to be produced from water, (2) conversion into a variety of fuels through many different reactions, (3) abundance of sources, (4) having high energy density³. At present, about 95 % of the H₂ consumed in the world is produced from fossil fuel by steam reforming of hydrocarbons; however, not only is this process extremely energy intensive, but it also emits greenhouse gases. From economic and environmental aspects, the generation of H₂ from renewable solar energy and water through photocatalytic water splitting is one of the most promising method⁴. Annually, the earth's surface obtains about 3×10^{24} J from solar irradiation, which is more than 100 times higher than the annual world consumption⁵. Photocatalysis has attracted extensive attention to the fields of environmental protection and clean energy and could be widely employed in many applications such as H₂ generation, air purification, and wastewater treatment. Photocatalytic water splitting by sunlight has gained significant attention in the scientific community because of its substantial possibility to solve the energy issue.

Though semiconductor photocatalysis has been investigated for several decades, its practical application is very limited. The major reason is the absence of a semiconductor that has the ability of the sunlight into chemical energy conversion efficiently⁶. As a result, finding suitable materials for photocatalytic processes is very demanding. Many attempts have been made until now to enhance the efficiency of this process. In this project, we are trying to use abundant and non-noble metal semiconductors for hydrogen production.

1.2. The scope of the thesis

Our goal in this project is the synthesis of cobalt oxides/mesoporous carbon nitride (MCN) for photocatalytic water splitting. Although carbon nitride (C_3N_4) is an ideal photocatalyst for water splitting, it has some drawbacks. Two ways to solve problems related to C_3N_4 are metal deposition and morphology control. MCN has a high surface area which leads to more active sites for reaction. Also, the optical properties can be increased upon deposition of metal. As a typical p-type nanostructured semiconductor with an exceptional electronic configuration and magnetic properties, cobalt oxide (CoO_x) has received substantial attention during recent years. Deposition of CoO_x into MCN could increase the efficiency and reduce the recombination rate. The specific research objectives are: 1) The synthesis of MCN and CoO_x /MCN; 2) Characterisation of these catalysts regarding the physical, structural, morphological and optical properties; 3) Evaluation of their photocatalytic activity in H_2 production.

1.3. The structure of the thesis

This brief introduction is followed by Chapter 2, which first explains the mechanism of photocatalytic water splitting and conventional materials which were used for this reaction. Then, C_3N_4 and its merits and demerits are introduced. MCN as a promising metal-free semiconductor is introduced. The reasons behind the necessity of MCN modification are discussed. In Chapter 3, synthesis of catalysts, characterisation techniques, and photocatalytic H_2 production tests employed throughout the thesis are described. In Chapter 4, the results related to MCN and Co_3O_4 /MCN characterisation and photocatalyst activity are analysed. In Chapter 5, the research outcomes, significance and ultimate impact of the work presented are summarised, and suggestions for future work are made.

Chapter 2: Literature Review

2.1. Mechanism of photocatalytic H₂ generation

The process of water splitting into H₂ over photocatalysts is shown in Figure 2-1⁷. For this process, a catalyst which is a semiconductor is normally used. The catalyst is activated by photons, which promote the transfer of an electron from the valence band (VB) to the conduction band (CB).

Due to electronic rights restrictions, this third party image has been suppressed from the digital thesis. Please see the citation listed below for further details on where the original image can be accessed

Figure 2-1 Schematic illustration of water splitting over semiconductor photocatalyst⁷.

When excited charges are generated, separation/migration and charge recombination are the two significant competing processes inside the semiconductor photocatalyst that largely impact the photocatalytic reaction efficiency⁵. The generated electrons are very unstable, and they have a tendency to recombine. If electron-hole carriers recombine, there is no reaction involved, just a release of energy. Otherwise, these carriers can contribute to the oxidation and reduction reactions and be captured by species to complete reactions. To have high efficiency, recombination should be hindered⁸. There are many methods to avoid recombination such as loading with co-catalysts⁹, using sacrificial agents¹⁰, and coupling with another semiconductor with different band gaps¹¹.

For overall water splitting, the electrochemical potential for the hydrogen evolution reaction (HER) is at 0 eV vs. normal hydrogen electrode (NHE) at pH = 0, and the electrochemical potential for the oxygen evolution reaction (OER) is at +1.23 eV vs. NHE, leading to a theoretical minimum band gap

of 1.23 eV that a semiconductor needs to perform this reaction¹². Figure 2-2 shows the band structure of various semiconductors and the redox potentials of water splitting.

Due to electronic rights restrictions, this third party image has been suppressed from the digital thesis. Please see the citation listed below for further details on where the original image can be accessed

Figure 2-2. Band levels of various semiconductor photocatalysts⁶.

Reactions which happen during photocatalytic water splitting are mentioned below:



Overall reaction:



where h is Planck's constant and ν is the frequency.

Fujishima and Honda in 1972 discovered overall water splitting over a titanium dioxide (TiO_2) electrode⁴. Since then, extensive studies have been done to enhance the activity of TiO_2 and to understand the reaction mechanisms. The following year they described the minimum requirements needed for water splitting, indicating that it was possible for the reaction to occur without the requirement for an external bias potential, thus marking the beginning of photocatalytic water splitting.

Semiconductors should meet several requirements to be suitable for photocatalytic water splitting. One of the most important features is a proper band gap, which determines the light absorption range. This property controls the ability of a semiconductor to undertake photoinduced electron transfer to the adsorbed species. For example, the lower the band gap, the higher the absorption of light. In addition to the band gap, the CB and VB positions of the semiconductor must be appropriate for the desired redox reaction. For example, in photocatalytic water splitting, VB must be appropriately positive to oxidize water for oxygen generation, and CB must be appropriately negative to be able to reduce water for hydrogen production. Since the ability of photocatalysis to utilise the solar energy as much as possible is very important, an efficient photocatalyst should absorb the sunlight effectively. The major portion of the solar spectrum is visible light which means that, to use the sunlight successfully, the semiconductor must have a band gap smaller than 3.0 eV. Another important property of photocatalysts is chemical stability and photo-corrosion resistance to avoid their decomposition during the reaction. The amount of active sites is a significant property that should be taken into account in photocatalysis. Being abundant and inexpensive are other properties of a suitable semiconductor to facilitate practical application finally.

2.2. Semiconductor materials for photocatalytic water splitting

2.2.1. TiO₂-based semiconductors

TiO₂ was the first semiconductor for photocatalytic water splitting⁴. Being chemically stable, safe to humans and the environment, photostable, easy to produce and cost-effective are some properties of TiO₂^{13,14}. The high significance of TiO₂ as a photocatalyst is because of its ability to oxidize a great number of organic compounds into harmless CO₂ and H₂O and to split water into oxygen and hydrogen¹⁵. This feature lies in its suitable electronic band structure. The valence band and the conduction band of TiO₂ are +2.53 and -0.52 eV, respectively, but there are several disadvantages related to this material. The band gap of TiO₂ (> 3.0 eV) limits its application to ultraviolet (UV) wavelengths, which comprises only 4 % of solar radiation. The main portion of the solar spectrum (45-50 %) is contributed by visible light, and finding a catalyst which could convert solar energy in this range is highly important.

Various strategies to improve the efficiency of TiO₂ have been applied so far. Controlling porosity as an ordered macroporous and mesoporous structures is the most extensively explored in TiO₂ photocatalysis because of having the abundance of active sites, high surface area, and easily accessible channels^{16,17}. Metal deposition into a TiO₂ structure reduces the recombination rate of electron-hole pairs which leads to better photocatalytic activity¹⁸. Another way is coupling with other semiconductors such as Ta₂O₅, WO₃, ZrO₂, and SnO₂ with TiO₂, which increases the charge separation and decreases the possibility of charge carrier recombination¹⁹. Dye sensitization of TiO₂ increases the efficiency as a photocatalyst by absorbing visible light²⁰. Doping metal and non-metallic nanoparticles into the TiO₂ structure decrease the energy gap by either raising the lower VB edge or dropping the upper edge of the CB²¹.

2.2.2. Other metal-oxide semiconductors

Besides TiO₂, some metal oxides have been investigated for water splitting due to their stability in aqueous solution and low cost. Among them could be mentioned Fe₂O₃²², ZnO²³, Ga₂O₃²⁴, and Co₃O₄²⁵. Similarly to TiO₂, most of them only absorb UV light because of their large band gaps. To improve their visible-light absorption, methods to increase the efficiency of TiO₂, including doping, controlling porosity, sensitizing, and coating different kinds of metal nanoparticles could be used equally with other oxides. Also, ternary metal oxide compounds such as Bi₂₀TiO₃₂²⁶, SnNb₂O₆²⁷, and BiVO₄²⁸ have been explored to overcome these limitations. Metal sulfides are considered as a good candidate for photocatalytic water splitting. Compared to metal oxides, they have a narrower band gap which increases their ability to absorb light²⁰. ZnS and CdS are the most considered metal sulfide photocatalysts over recent years²⁹.

Transition metal oxide nanoparticles show an important class of inorganic nanomaterials that have been explored widely because of their interesting magnetic, electronic, and catalytic properties relative to those of the bulk counterparts, and wide scope of their potential applications³⁰. Among them, cobalt oxide has attracted a great deal of attention. There are three types of cobalt oxides, i.e., Co₃O₄ with a spinel structure, CoO with a rocksalt structure, and Co₂O₃ with a hexagonal structure³¹. In particular, tricobalt tetraoxide (Co₃O₄), a p-type semiconductor, has been explored as a promising material in heterogeneous catalysts³², gas sensors³³, electrochemical devices³⁴, Li-ion batteries³⁵, magnetic

materials³⁶, and photocatalysts³⁷. The spinel cobalt oxide Co_3O_4 is a magnetic semiconductor containing cobalt ions in Co^{3+} and Co^{2+} oxidation states³⁸.

2.2.3. Metal-free materials

Metal-free semiconductors have appeared as a new generation of visible-light-driven photocatalysts. In spite of the improvement in the field of metal-based semiconductors, they still suffer from some problems like corrosiveness, toxicity, and instability³⁹. The metal-free photocatalysts studied up to now consist of earth-abundant elements, such as N, C, P, S, etc. Phosphorus is an interesting material as a photocatalyst for H_2 production³⁹. Among its three allotropes (red, white and black), black and red phosphorus have been reported for a photocatalytic H_2 generation. Different types of carbon-based materials such as carbon dot⁴⁰, carbon nanotube⁴¹, and graphene oxide⁴² have been studied for photocatalyst processes.

Carbon dots (CDs) are of particular interest as a new generation of materials for photocatalysis. CDs are provided with a varying range of optical properties and performance parameters because of the variety of synthetic methods and materials. Different kinds of CDs, which are all attributed to the 0D carbon-based nanomaterials, have similar nontoxic, water-soluble, easily prepared, environmentally friendly, photo-stable and tunable fluorescent properties⁴³. CDs can generate e^-/h^+ pairs under light irradiation with the advantages of non-toxicity, low cost and unique photoelectric properties⁴⁴. Carbon nanotubes (CNTs), generally as form of single-walled carbon nanotubes (SWCNTs) and multi-walled carbon nanotubes (MWCNTs), gain substantial attention because of their distinct structure and high mechanical strength which makes them suitable options for advanced composites. Based on the structure and shape, CNTs conduct electricity due to delocalization of the π -bond electrons⁴⁵. Graphene, a single layer of sp^2 -bonded carbon atoms, has a large exposed area and a p-conjugation structure that shows outstanding electronic mobility⁴⁶. These properties make graphene a viable co-catalyst to accept electrons for exciton separation. Though, graphene sheets are hydrophobic and unsuitable for direct use in water splitting⁴². The physicochemical properties of graphene oxide (GO) can be tuned by engineering its atomic and chemical structures⁴⁷. From a wider viewpoint, the promising properties such as hydrophilic and tunability inherent to GO sheets are very promising for facilitating a different range of applications and shows remarkable performance in photocatalytic water splitting^{48,49}.

Compounds of carbon and nitrogen, known as carbon nitrides (C_3N_4), have been shown to have promising properties for photocatalytic water splitting. The visible-light photocatalytic activity of C_3N_4 for H_2 production in the presence of a sacrificial donor was discovered by Wang et al.⁵⁰. Because of several features like being metal-free, nontoxic, low-cost, chemically stable, C_3N_4 has attracted worldwide attention. At ambient conditions, graphitic carbon nitrides ($g-C_3N_4$) are regarded to be the most stable allotrope. The N links the rings in the end to form an infinite plane⁵¹. Generally, C_3N_4 has been synthesised through thermal condensation from nitrogen-rich precursors like urea⁵², cyanamide⁵³, melamine⁵⁴, and 3-amino-1,2,4-triazole⁵⁵. The composition, crystallinity, and structure of C_3N_4 control the properties of C_3N_4 materials⁵⁶. The raw materials for the synthesis of $g-C_3N_4$ are various and easily accessible. The process of high-temperature polymerisation is the key reactions for the precursor. This reaction for cyanamide is shown in Figure 2-3 (a)⁵⁷. Polyaddition and polycondensation are the two main reactions. Firstly, the precursors polymerise to melamine. Then condensation happens by removing ammonia from melamine to form the $g-C_3N_4$ polymer. $g-C_3N_4$ is a two-dimensional sheet containing of triazine groups (Figure 2-3 (b)) and is the most stable allotrope⁵⁰.

Due to electronic rights restrictions, this third party image has been suppressed from the digital thesis. Please see the citation listed below for further details on where the original image can be accessed

Figure 2-3. (a) Reaction pathways for the formation of $g-C_3N_4$ using cyanamide⁵⁷, (b) Scheme of triazine-based connection in $g-C_3N_4$ ⁵⁰.

$g-C_3N_4$ has similar π -conjugated planar layers to that of graphite, which makes it possess high stability against thermal and chemical attacks and an appealing electronic structure⁵⁸. During the past decade,

the use of C_3N_4 for various applications like fuel cell and photocatalysis, as well as CO_2 capture and heterogeneous catalysis, has increased progressively. The band gap of C_3N_4 is about 2.7 eV, which is tunable by the amount of nitrogen in the C_3N_4 structure. This quantity is related to the synthesis temperature and the type of precursor. The band structure of g- C_3N_4 is shown in Figure 2-4⁵⁹. It can be concluded from the figure that g- C_3N_4 possesses the required band positions of the CB and VB (CB=- 1.3eV, VB=1.4eV vs. NHE, pH=7) for photocatalytic water splitting.

Due to electronic rights restrictions, this third party image has been suppressed from the digital thesis. Please see the citation listed below for further details on where the original image can be accessed

Figure 2-4. The band energies of g- C_3N_4 and TiO_2 , a relative to the redox reactions of water and photoemission energies⁵⁹.

Controlling the CB and the VB position of C_3N_4 by changing the amount of nitrogen is a challenging research area. The improvement of the photocatalytic performance of g- C_3N_4 by changing the design of the nanostructure is a promising method. Various structures such as bulk C_3N_4 , C_3N_4 nanosheets (C_3N_4 NSs) and C_3N_4 nanotubes (C_3N_4 NTs) have been synthesised^{60,61}. Compared to bulk C_3N_4 and C_3N_4 NSs, C_3N_4 NTs have higher performance, which could be related to sufficient active sites, high photogenerated carrier transfer efficiency and better mass transfer capability⁶⁰. In spite of the mentioned fascinating properties of C_3N_4 , some disadvantages like low surface area, high recombination rate and visible-light absorption limitation beyond 460 nm limit the usage of this material for practical applications⁶². Recently, many methods have been proposed to overcome these shortcomings such as metal doping⁶³, nonmetal doping⁶⁴, modification with conductive materials⁶⁵, morphology control⁶⁶, and coupling with other semiconductors⁶⁷.

2.3. Mesoporous carbon nitride (MCN)

Morphology control *via* synthesis of a mesoporous structure has gained attention during recent years. There are several methods for the synthesis of mesoporous materials such as the soft and hard templating approaches. Having abundant active sites, high surface areas and readily accessible channels are the properties of porous materials, which are favorable for promoting the diffusion of reactants and products, showing a promising class of structure for photocatalysis application⁶⁸. Based on the definition of the International Union of Pure and Applied Chemistry (IUPAC), porous solids are categorized into three classes based on their pore diameter (d), namely microporous (pore size < 2 nm), mesoporous (pore size 2-50 nm), and macroporous (pore size > 50 nm) materials. Macroporous and mesoporous g-C₃N₄ were prepared by soft- and hard-templating methods, as shown in Figure 2-5⁶⁹.

Due to electronic rights restrictions, this third party image has been suppressed from the digital thesis. Please see the citation listed below for further details on where the original image can be accessed

Figure 2-5. Scheme of two major routes for the synthesis of MCN: (a) soft-templating and (b) hard-templating method⁶⁹.

2.3.1. Synthesis of MCN

2.3.1.1. Hard-templating method

The hard template approach has been used widely for MCN synthesis due to accurate morphology control, uniform pore structure, highly ordered nanopores and excellent thermal stability. By synthesis of the porous material via templating strategies, problems related to the low surface area and the pore volume could be solved. These properties give a high number of active sites, strong adsorption ability and higher selectivity toward the desired product, which lead to better performance. Porous materials

may curtail the migration distance and reduce the recombination possibility. Figure 2-6 summarises the application of MCN, its properties and ways to fabricate MCN⁵⁶.

Due to electronic rights restrictions, this third party image has been suppressed from the digital thesis. Please see the citation listed below for further details on where the original image can be accessed

Figure 2-6. Overall scheme for the synthesis, functionalisation, and applications of the MCN⁵⁶.

Silica is usually used as a template and is removed at the end of the reaction by mixing with de-template agents such as hydrogen fluoride (HF) and ammonium hydrogen fluoride (NH₄HF₂). The type of silica for a hard template could affect different properties of MCN such as the structure. Using silica nanoparticles leads to MCN with a disordered spherical morphology and using synthesised SBA-15 leads to MCN with an ordered rod-like morphology. Figure 2-7 shows the synthesis of MCN via two different silica templates⁷⁰.

Due to electronic rights restrictions, this third party image has been suppressed from the digital thesis. Please see the citation listed below for further details on where the original image can be accessed

Figure 2-7. Synthetic pathways to MCN through hard-templating methods⁷⁰.

Template synthesis, the temperature of carbonisation, the mass ratio of template to precursor and the type of precursor affect the physical, morphological, optical and structural properties and performance of MCN. Luo et al. investigated MCN for RhB photocatalytic degradation⁷¹. KIT-6 silica was used as a hard template. They investigated the mass ratio of KIT-6 silica to melamine as a precursor. With an increasing ratio of KIT-6 to melamine from 0 to 80 %, the surface area increased from 15.1 to 279.3 m²/g. Further increasing caused a decrease in surface area. The lowest recombination rate and highest photogenerated charge carriers separation and photo-absorption were obtained when the ratio of KIT-6 silica to melamine was 80 %. This sample had the highest activity and degraded RhB totally within 50 min. Urea was used as a precursor to synthesise MCN by Lee et al.⁵². They investigated the effect of the mass ratio of urea to silica on the morphology of the MCN, the pore-size distribution, and the specific surface area. There is no clear correlation between specific surface area and the mass ratio of urea to silica. Silica washing could cause pore collapse, and as a result low surface area, especially when the ratio of urea to silica was too low, and the morphology of sample is worm-shaped structures like bulk carbon nitride. Samples which have higher surface area showed the better photocatalytic removal of phenol. When the mass ratio of urea to silica was too high, the surface area is low because of the decreased formation of MCN due to the growth of CN without template confinement.

Park et al. prepared MCN from 3-amino-1, 2, 4-triazole as a single molecular carbon and nitrogen precursor for CO₂ capture⁷². KIT-6 silica as a template was synthesised at 100, 130, and 150 °C. From the XPS results, it can be concluded that the temperature of template synthesis plays a key role in the content of nitrogen of MCN. The amount of nitrogen increased at elevated temperature. At a higher temperature for template synthesis, the specific surface area and pore diameter increased. The proposed stoichiometry for MCN fabricated at 150 °C is C₃N_{5.09}, and also this sample had the highest CO₂ adsorption capacity. The amount of CO₂ adsorption is a function of the pore diameter, specific surface area, and nitrogen content. Long et al. studied the effect of the synthesis temperature of the SBA-16 silica template on photocatalytic water splitting⁷³. MCN was prepared from SBA-16 and liquid cyanamide as a hard template and precursor. Figure 2-8 shows H₂ generation for MCN synthesised from SBA-16 silica at various temperatures. The higher the synthesis temperature of the template, the better the separation of photoinduced charge carriers and the higher the number of surface active sites, thus the higher the H₂ rate. Also, the effect of electron donors in terms of H₂ evolution was studied. Different donors such as triethanolamine (TEOA), ethanol, methanol and ethylenediaminetetraacetic acid (EDTA) were tested. When TEOA was used, the highest yield of H₂ evolution observed. This result suggests that TEOA is an effective hole scavenger in the test system.

Due to electronic rights restrictions, this third party image has been suppressed from the digital thesis. Please see the citation listed below for further details on where the original image can be accessed

Figure 2-8. H₂-evolution by CN-SBA-16-T samples as a function of reaction time⁷³.

Talapaneni et al. synthesised MCN using aminoguanidine hydrochloride and mesoporous silica SBA-15 as a hard template⁷⁴. The N/C ratio of the fabricated MCN (1.80) was significantly higher than that

of the theoretically predicted C_3N_4 nanostructures (1.33) because it easily undergoes polymerisation at high temperatures and affords a highly stable polymer composed of a diamino-s-tetrazine moiety with a six-membered aromatic ring comprising six nitrogen atoms. The pore diameter of MCN increased as the synthesis temperature of the silica SBA-15 went up. Pore diameter plays a key role in the amount of nitrogen due to the difference of pore filling and the nature of the structural order in the materials. The higher the pore diameter, the higher nitrogen content. The UV-Vis spectra of samples confirmed that the band gap of MCN could change by simply adjusting the content of the nitrogen or the pore diameter of the sample. Talapaneni et al. used two sources for nitrogen and carbon for the synthesis of MCN⁷⁵, with mesoporous silica KIT-6 as a hard template. Ethylenediamine and carbon tetrachloride were used as the sources for N and C, respectively. The BET and BJH results show bimodal pores. The small mesopores could be related to the removal of the silica template, whereas the complementary mesopores are assumed to originate from either partial filling of the pores deep inside the materials with the C and N precursors that creates large empty pores before the removal of silica or the coalescence of the mesopores. The catalytic activity of MCN was tested on the base catalyzed Knoevenagel condensation of benzaldehyde and malononitrile. Samples show high activity, leading to excellent yield to the desired product. This could be related to high surface area, mesoporous structure, and large pore volume with a great number of strong basic sites which come from nitrogen functional groups.

Tian et al. synthesised MCN via dissolving dicyandiamide as a precursor into various solvents such as N,N-dimethylformamide (DMF), water, or ethanol. SBA-15 was used as a template⁷⁶. As can be found from Figure 2-9, the sample which was prepared in DMF has a better performance of the catalytic dehydrochlorination of 1,1,2-trichloroethane into 1,1-dichloroethene reaction for conversion and selectivity. This could be attributed to the fact that using DMF as a solvent can bring extra N groups into the CN structure in the form of NH_2 groups attached to the tri-s-triazine structure, which leads to the better performance of MCN.

Due to electronic rights restrictions, this third party image has been suppressed from the digital thesis. Please see the citation listed below for further details on where the original image can be accessed

Figure 2-9. Catalytic performance of MCN prepared by using various dispersing solvents for MCN fabrication⁷⁶.

Vinu et al. studied the effect of carbonisation temperature on MCN synthesis from 600 to 1000 °C for CO₂ adsorption⁷⁷. They found that this parameter plays a key role in controlling the crystallinity and the nitrogen content, as well as the surface area and pore volume. As the carbonisation temperature increased, the nitrogen content of MCN reduced and the crystallinity of the samples, the surface area, and the pore volume increased. With rising carbonisation temperature, CO₂ adsorption capacities improved until 900 °C. It could be summarized that samples with the optimum nitrogen content, high specific surface area and pore volume are the best adsorbents for CO₂. It is quite clear from this study that there is a synergistic interplay between the textural properties and nitrogen content. CO₂ adsorption capacity is strongly influenced by textural parameters. Vinu et al. report a new MCN with C₃N₅ stoichiometry that has a higher nitrogen content than the predicted C₃N₄ stoichiometry for photocatalytic water splitting⁵⁵. This material was synthesised from a single-molecular precursor with a high nitrogen content, 3-amino-1, 2, 4-triazole (3-AT). The cyclic aromatic precursor plays a key role because of keeping a high amount of nitrogen in the carbon matrix. TEM images and nitrogen adsorption-desorption isotherms approved the formation of mesoporous structure with a pore size of 3.42 nm and a specific surface area of 296.7 m²/g. This material has a low band gap energy (2.2 eV), which is substantially lower than the bulk g-C₃N₄ band gap (2.7 eV) and enables high absorption of visible light. This property gives C₃N₅ a high efficiency for hydrogen evolution without using any co-catalysts.

2.3.1.2. Soft-templating method

The hard template approach is not suitable for an industrial scale because of the high cost and toxicity to humans and the environment. The soft template method is normally used for organic molecules like amphiphilic polymer, a surfactant as a template. The benefit of using this method is an easy operation, simple equipment, and low cost. However, as a drawback of this method could be not controlling the size and morphology of the mesoporous material, which leads to lower catalyst performance.

Fan et al. synthesised MCN by using melamine and glutaraldehyde as precursors and surfactant Triton X-100 as the soft template through polymerisation and carbonisation⁷⁸. The sizes of the mesoporous in the product were centered at 3.8 and 10-40 nm. With bimodal pore distribution, the former one is because of the removal of Triton X-100 at the end of synthesis during the carbonisation process and the latter probably derived from the aggregates of plate-like particles of carbon nitrides. This MCN showed a high capacity for *Candida rugosa* lipase adsorption which could be ascribed to its mesoporous structure and also N functional bonds in the MCN structure such as C-N and N-H, connecting with the oxygen-containing groups, endowing its surface with a polar nature. Yan synthesised MCN using melamine and Pluronic P123 as a precursor and soft template, respectively⁷⁹. The photocatalytic activity of MCN with 10 wt% P123 as template was much higher than that of g-C₃N₄ without using the template. Further increasing the amount of P123 leads to a minor increase in the photocatalytic H₂ evolution (Figure 2-10). This shows the positive effect of the P123 surfactant which leads to increasing BET surface area and promotes the red shift of optical absorbance wavelength up to 800 nm.

Due to electronic rights restrictions, this third party image has been suppressed from the digital thesis. Please see the citation listed below for further details on where the original image can be accessed

Figure 2-10. The rate of H₂ evolution on MCN prepared with different mass ratio of P123 to melamine under visible-light irradiation⁷⁹.

2.3.2. Surface modification of MCN

Although MCN has a high surface area, it still suffers from weak visible-light absorption and a high recombination rate. These disadvantages have restricted the usage of MCN. One approach to overcome these problems is the surface modification of MCN with metal oxide semiconductors. Due to the presence of sp²-hybridized nitrogen atoms which can act as a scaffold, metal nanoparticle co-catalysts could be well dispersed on the surface of g-C₃N₄⁶¹. Different benefits such as a decreased rate of recombination, increased the range of the wavelength photoresponse into the visible region of the spectrum, changed selectivity for desired products, enhancement of surface properties and increased stability of the semiconductor have been reported with modification of the semiconductor⁵⁶. Noble and non-noble metal deposition onto the surface of MCN has attracted a lot of attention so far.

2.3.2.1. Surface modification by noble metal nanoparticles

Dai et al. fabricated Au/MCN and Au/activated carbon (AC) for acetylene hydrochlorination⁸⁰. The TEM images have verified the idea of size-controlling MCN and the role of MCN in dispersing metal nanoparticles uniformly⁷⁷. Au particles dispersed very well on the surface of MCN with a mean particle size of 5 nm, while the Au nanoparticles were agglomerated on the outside surface of the AC with an average particle size of 16 nm. Regarding the activity, Au/MCN showed better performance than Au/AC because of the low particle size of Au and also interaction between the active component and the support. Vinu et al. fabricated Au nanoparticles/MCN⁸¹. After the support of Au on the surface

of MCN. The functional group (-NH₂ and -NH) acts as a platform for the formation of metal and metal oxide nanostructure. FE-HRSEM and HRTEM images showed that Au particles were dispersed on the surface of MCN uniformly and without any agglomeration which can be seen from Figure 2-11 (a) and (b). The size of the Au particles was estimated to be around 7 nm, which has an agreement with the size of MCN pore diameter. Au was supported on mesoporous carbon (MC) in order to test the functional group on the surface of MCN which are absent in MC. The HRSEM image presented in Figure 2-11(c) showed that the particle grew on the external surface of MC rather than on the internal surface. Also, the range of Au size was from 20 to 140 nm. The result reveals the important role of nitrogen in the MCN matrix. Au/MCN was used as a selective, highly active and reusable heterogeneous catalyst for coupling benzaldehyde, piperidine, and phenylacetylene for the synthesis of propargylamine.

Due to electronic rights restrictions, this third party image has been suppressed from the digital thesis. Please see the citation listed below for further details on where the original image can be accessed

Figure 2-11. a) FE-HRSEM, b) HRTEM images of Au nanoparticle encapsulated MCN and c) HRSEM image of Au nanoparticle encapsulated AC⁸¹.

Sasidharan et al. prepared Pd nanoparticles on MCN with two methods which led to different oxidation states named Pd(0)-MCN and Pd(II)-MCN⁸². The BET surface areas for Pd(0)-MCN and Pd(II)-MCN were 329 m²/g and 356 m²/g, respectively. TEM images showed that Pd nanoparticles distributed uniformly across the hexagonal mesoporous channels for both samples. Wang et al. reported Pd/MCN for the direct hydrogenation of phenol to cyclohexanone⁸³. They used cyanamide and Ludox HS40 as a precursor and silica template, respectively. It was observed from the TEM, HRTEM and STEM images presented in Figure 2-12 that the Pd particles were dispersed very well.

This catalyst showed high conversion and selectivity (around 99 %). The effect of various solvents for the reaction was studied as well. Between the tested solvents, water and CH_2Cl_2 showed the highest activity. Using ethanol gave high activity but with a low selectivity toward cyclohexanone.

Due to electronic rights restrictions, this third party image has been suppressed from the digital thesis. Please see the citation listed below for further details on where the original image can be accessed

Figure 2-12. (a) STEM, (b) HRTEM, and (c) TEM images of Pd/MCN⁸³.

Wang et al. investigated the loading of Pt on MCN for oxidation of glycerol⁸⁴. They used ethylenediamine (EDA) and carbon tetrachloride (CTC) as a source of nitrogen and carbon to synthesise MCN, respectively. The MCN was fabricated with different nitrogen contents by changing the addition mass of EDA. By enhancing the N content, the Pt particle sizes slowly reduced. It could be concluded that MCN was obtained from precursors which have inherent $-\text{NH}$ and $-\text{NH}_2$ groups on the mesoporous walls. These groups can perform as a stabilizing agent by providing an anchoring and heterogeneous surface that allows the formation of highly distributed metal nanoparticles without any agglomeration. The existence of more functional amine groups on MCN helps to decrease the aggregation of Pt nanoparticles and stabilize the formed nanoparticles inside the mesoporous channels. From the temperature programmed desorption (TPD) test, the higher the N content, the more number of weak basic sites. For all of the Pt/MCN catalysts, the conversion of glycerol improved with increasing N content in the catalysts, indicating that more basic sites promote the oxidation of glycerol. Pt-Ru/MCN for direct methanol fuel cells (DMFC) was synthesised by Bello et al.⁸⁵. They used EDA and CTC as nitrogen and carbon precursors, respectively. MCN with different pore diameters which is the result of different temperatures for the synthesis of silica template were impregnated with Pt and Ru nanoparticles, which were employed as electrodes for DMFC. The electrocatalytic activity of

Pt-Ru/MCN showed higher activity than commercial catalysts which could be ascribed to high surface areas, large pore volumes, and uniform pore size distribution with free NH₂ functional groups on the walls of pores.

2.3.2.2. Surface modification by non-noble metal nanoparticles

Le et al. explored the effect of Cu-doping into the MCN on the photocatalytic degradation of methyl orange (MO) under visible-light irradiation⁸⁶. Cupric chloride, melamine and SBA-15 were used as precursors and template, respectively. It was observed that the light absorption of the Cu/MCN was enhanced in comparison with the bare MCN and also the electron/hole separation rate with added Cu²⁺ increased, leading to better photocatalytic performance. They studied the effect of copper amounts in the MCN structure up to 5 %. The higher the amount of copper, the better catalytic performance. This result could be related to the amount of surface area. The higher copper amounts into MCN structure, the higher surface area. Qiu et al. fabricated Co₃O₄/MCN for degradation of bisphenol A (BPA)⁸⁷. The XPS results showed that the cobalt species loaded on MCN samples were Co₃O₄. It was found that loading Co₃O₄ into MCN structure suppressed the recombination of the electron-hole pairs, increased noticeably the separation efficiency of photoinduced electrons-holes and higher light absorption (Figure 2-13). Thus, the photocatalytic efficiency of Co₃O₄/MCN was much higher compared with MCN.

Due to electronic rights restrictions, this third party image has been suppressed from the digital thesis. Please see the citation listed below for further details on where the original image can be accessed

Figure 2-13. (a) Photoluminescence spectra, (b) Photocurrent measurements, (c) UV-vis diffuse reflectance spectra of g-C₃N₄, mpg-C₃N₄ and 1.5 % Co₃O₄/mpg-C₃N₄⁸⁷.

Guo et al. synthesised potassium and iodine co-doping with MCN via the one-pot thermal polymerisation using potassium iodide and dicyandiamide as the dopant and precursor, along with SBA-15 silica as a hard template⁸⁸. Due to the synergistic effect of the K and I doping with the mesoporous structure, several properties such as the absorption band, the lifetime of carries, the charge transport, and the photocurrent density were enhanced. The H₂ generation for MCN doped with K and I was 9.7 times as high as for the bare MCN. Liang et al. prepared binary metal sulfide/MCN for degradation of rhodamine B (RhB) and methylene blue (MB) under visible light irradiation⁸⁹. The synthesis of SnCoS₄/MCN as demonstrated in Figure 2-14 includes two steps, preparation of MCN and loading SnCoS₄ on the MCN structure. The results showed that SnCoS₄/MCN has a wide absorption edge in the whole visible light region and a low rate of electron-hole pairs recombination compared with pristine SnCoS₄ and MCN. Photocatalytic degradation of RhB and MB on SnCoS₄/MCN was much higher than MCN attributing to the formation of n-n type heterojunction, prohibited the recombination of electron-hole and the intimate synergistic interactions.

Due to electronic rights restrictions, this third party image has been suppressed from the digital thesis. Please see the citation listed below for further details on where the original image can be accessed

Figure 2-14. Graphic design for preparation of SnCoS₄/MCN⁸⁹.

Li et al. used 1-butyl-3-methylimidazolium tetrafluoroborate (BmimBF₄), an ionic liquid, as a soft template and precursor for boron and fluorine, and dicyandiamide (DCDA) as a source of carbon and nitrogen⁹⁰. The ratio of the template to precursor could affect the surface area of MCN and the nitrogen content. The resulting materials showed a narrow pore size distribution and high absorption in the visible range, which leads to a high catalytic activity for the selective oxidation of cycloalkanes. The catalysts afford a significantly high selectivity towards cyclohexanone formation. They were highly

stable and could be reused several times. Thinda et al. studied TiO₂ supported on MCN⁹¹. TEM images showed that the C₃N₄-TiO₂ nanocomposite had a lower particle size and a smaller pore diameter compared to C₃N₄ due to the formation of TiO₂ which prevented the growth of C₃N₄ crystal. The surface area of C₃N₄-TiO₂ (12 %) was 138 m²/g which is higher than that of the bare C₃N₄ (73.0 m²/g). The band gap of the nanocomposite was less than that of C₃N₄ (~2.8 eV) and TiO₂ (~3.2 eV) samples, leading to a high visible light response. This was related to the synergistic effect that was achieved due to the surface interactions between C₃N₄ and TiO₂, as well as the formation of the integrated C₃N₄-TiO₂ nanocomposites. The photocatalytic degradation of RhB under visible light for C₃N₄-TiO₂ (12 %) was higher than bare C₃N₄, which could be related to the increase of light absorption, photocurrent density and the decrease of electron-hole recombination.

Xu et al. fabricated sulfur-doped MCN (mpgCNS), using thiourea as a precursor and SiO₂ nanoparticles as the hard template for photocatalytic H₂ evolution⁹². They used an in situ method for sulfur doping. A mechanism for the formation of mpgCNS was proposed (Figure 2-15). The TEM images showed that mpgCNS had pores with a diameter of 10-20 nm which matched with the size of the SiO₂ template and also agree with the pore size distribution profile. Sulfur doping in MCN enhanced the light absorbance in both the UV and visible light regions. mpgCNS was 30 times more active than the bare g-C₃N₄ for photocatalyst water splitting as a result of the effect of stronger and extended light absorbance in the visible light region by sulfur doping and more charge transfer and efficient mass in the mesoporous structure.

Due to electronic rights restrictions, this third party image has been suppressed from the digital thesis. Please see the citation listed below for further details on where the original image can be accessed

Figure 2-15. Formation mechanism of mpgCNS⁹².

Kailasam et al. synthesised tungsten oxide on MCN with using Pt as a co-catalyst and applied for photocatalytic H₂ evolution⁹³. WO₃/MCN composites were prepared by dispersing WO₃ powders with MCN via impregnation method. WO₃/MCN showed a very high photocatalytic H₂ generation water under visible light, because of the high surface area and a synergetic effect between the carbon nitrides and the WO₃, which led to enhanced charge separation through a photocatalytic mechanism as shown in Figure 2-16. After modification with WO₃, the photoinduced holes in the VB of g-C₃N₄ and the photogenerated electrons in the CB of WO₃ recombine at the interface, leaving the electrons in the CB of g-C₃N₄ and holes in the VB of WO₃. As a result, the overall charge separation was improved which lead to higher photocatalytic activity.

Due to electronic rights restrictions, this third party image has been suppressed from the digital thesis. Please see the citation listed below for further details on where the original image can be accessed

Figure 2-16. Schematic diagram of the photocatalytic mechanism in WO₃/MCN⁹³.

Xu et al. synthesised vanadia/MCN catalysts using NH₄VO₃ as a precursor and MCN as support via a wet impregnation method⁹⁴. The vanadia/MCN catalysts exhibited significant catalytic activity in the hydroxylation of benzene to phenol in the existence of H₂O₂. The high catalytic activity is ascribed to the high benzene-activation MCN capability and good distribution of the vanadia types into MCN structure. Because of having the inbuilt and unique tri-s triazine moieties, MCN adsorbed chemically and then activated benzene on the catalytic surface, through an electron migration from HOMO of C₃N₄ to LUMO of benzene, where MCN materials presenting high surface areas and rich pores increased the amount of adsorbed benzene molecules.

Luo et al. synthesised iron oxides/MCN for phenol oxidation⁹⁵. They used ferric nitrate and melamine as a source of iron and C₃N₄ precursor, respectively. The mass ratio of SiO₂ to melamine was studied.

When the ratio is 30 %, the surface area is highest due to the inclusion of the silica nanoparticles during synthesis. Too much silica template, however, leads to a framework collapse that reduces the surface area. After loading iron, a sample in which the ratio was 30 % shows the highest surface area and the highest activity for phenol oxidation. It could be inferred that the surface area has a great influence, not only on the dispersion of FeO_x but also on the mass diffusion of the reactant during phenol oxidation. Fang et al. synthesised AgBr nanoparticles loaded on MCN via a simple adsorption–deposition method, for degradation of methyl orange (MO) dye⁹⁶. They used amino cyanide solution and a colloidal silica solution as the reaction precursors. Optical properties such as absorption and photocurrent were increased after loading of AgBr on MCN. As a result, AgBr/MCN has a higher activity for degradation of MO than bare MCN.

Regarding its features, using MCN in different applications specially photocatalytic H_2 generation has been studied and gained a great deal of attention. To improve activity, different kind of metals including noble metals and non-noble metals have been used as a co-catalyst. Regarding research which has done until now, using supporting Co_3O_4 as a co-catalyst on MCN for photocatalytic water splitting has not been reported so far.

Chapter 3: Experimental Section

3.1. Materials and chemicals

3-amino 1, 2, 4-triazole, ammonium bifluoride (NH_4HF_2), cobalt acetate and SiO_2 particles (Ludox HS40) were purchased from Sigma-Aldrich. Methanol was purchased from Chem-Supply. Hydrogen chloride (HCl) (36 %) were purchased from RCI Labscan. All the chemicals were used as received without further purification.

3.2. Catalyst preparation

3.2.1. MCN fabrication

MCN was fabricated as reported with a few changes⁵⁵. 3.0 g of 3-amino 1, 2, 4-triazole was mixed in 5 ml of deionized (DI) water and 0.5 mL HCl. The mixture was kept under stirring for 5 min at 50 °C. Once complete dissolution was achieved, it was thoroughly mixed with 6 mL of 40 wt% of SiO_2 particles (Ludox HS40, Aldrich) used as a hard template, and the obtained mixture was stirred at 80 °C for 2 h. The composite of silica template and partially condensed 3-amino 1, 2, 4-triazole was transferred to a crucible and calcined with a ramp of 10 °C/min up to 500 °C and kept at this temperature for another 4 h in N_2 . The resultant yellow powder was treated with 4 M NH_4HF_2 solution and stirred for 24 h at room temperature to dissolve the silica template. The template-free MCN obtained was centrifuged and washed with DI water and ethanol several times and dried at 75 °C overnight. MCN with various ratios of silica template to the precursor were synthesized for comparison.

3.2.2. Co_3O_4 fabrication

A suitable amount of cobalt acetate was dispersed in 50 mL of ethanol. After that the solution was stirred overnight. The prepared solution was then dried at 60 °C for 2 h. Finally, the dried powder was sintered at 300 °C for 2 h with a heating rate of 10 °C/min in vacuum and cooled naturally to room temperature.

3.2.3. Co₃O₄/MCN fabrication

Co₃O₄/MCN catalysts with different percentage of Co₃O₄ were prepared by the conventional impregnation method⁹³. The Co₃O₄ powder was dispersed in ethanol (5 mL) and mixed with a slurry containing the respective MCN (0.10 g) dispersed in ethanol (15 mL). The resulting mixture was stirred at room temperature overnight. The ethanol was removed by evaporation at 85 °C. Finally, a thermal treatment in argon at 100 °C for 2 h was performed, leading to the final Co₃O₄/MCN composites. The products were defined as x-Co₃O₄/MCN where x stands for the mass percent of Co₃O₄/MCN.

3.3 Characterisation

X-ray diffraction (XRD) patterns were obtained using a PANalytical X'Pert PRO diffractometer via Cu K α 1 radiation at a scan speed of 4° min⁻¹ from 10 to 80° for wide-angle and a scan speed of 0.045° sec⁻¹ from 0.5 to 5° for low-angle. For determination of the amount of cobalt, microwave plasma – atomic emission spectroscopy (MP-AES, Agilent 4100 MP-AES) was used. 50 mg of sample was solved by 12 mL of sulfuric acid (H₂SO₄) and hydrogen peroxide (H₂O₂) (3:1 v/v) and then was heated at 80 °C for 2 h and making volume up to 100 mL by adding DI water. The Brunauer-Emmett-Teller (BET) specific surface area and pore size distribution of the samples were performed by N₂ adsorption/desorption using a Micrometrics Tristar 3000 with the BET and Barrett-Joyner-Halenda (BJH) methods, respectively. Scanning electron microscopy (SEM) with energy-dispersive X-ray spectroscopy (EDX) was conducted on a JCM- 6000PLUS at a voltage of 15 kV. Transmission electron microscopy (TEM) images were obtained using a JEOL-2100F microscope operating at 200 kV, by depositing a drop of sample suspension onto 300-mesh copper grids. Al K α X-ray radiation source (E =1486.68 eV). The ultraviolet-visible (UV-vis) diffuse reflectance spectra were recorded on a Varian Cary 500 Scan UV-vis spectrophotometer. FT-IR spectra were recorded by a Nicolet 6700 FT-IR spectrometer with a 4 cm⁻¹ resolution and 32 scans in the range of 4000-600 cm⁻¹. Photoluminescence (PL) measurements were carried out on a Fluorolog-Tau3 fluorescence spectrophotometer with an excitation wavelength of 330 nm at room temperature.

3.4 Evaluation of photocatalytic H₂ production

The visible-light illumination was achieved by eliminating the UV part of the spectrum from a 300 W xenon arc lamp using a 420 nm cut-off filter. In a typical experiment, 40 mg of the prepared catalysts was dispersed in 40 mL of deionized water containing 10 vol % of triethylamine (TEA) as a sacrificial reagent. The light source was fixed about 30 cm from the liquid surface of the suspension. Before irradiation, the system was vacuumed for 15 min and then purged with Argon gas for 15 min and maintained in an Argon atmosphere. Then, the solution was irradiated from the top through a quartz window under stirring, and an external cooling jacket was used to absorb the heat. During the irradiation, the resulting gas was analysed every 30 min using a gas chromatograph (GC 2014; Shimadzu Corporation) equipped with a thermal conductivity detector and a 5 Å molecular sieve column and with N₂ as a carrying gas.

3.5 Electrochemical measurement

In order to study the mechanism of photocatalysis, photoelectrochemical measurements were performed on a potentiostat (SP-300, BioLogic Science Instruments) in a conventional three-electrode configuration with a Ag/AgCl (in saturated KCl) and Pt-wire as a reference electrode and counter electrode, respectively, and all potentials converted to the NHE reference scale. 8 mg of catalyst was dispersed into 2 mL of a water-isopropanol mixed solvent (4:1 v/v). Then, 4 µL of nafion was added into the solution and sonicated for at least 30 min to form a homogeneous suspension. For the measurements, 40 µL of the catalyst suspension was deposited onto Ti foil to form the working electrode. The electrolyte was 0.5 M Na₂SO₃ aqueous solution (100 mL). The photocurrent measurements were carried out at a constant potential of +1.0 V, and a 300 W Xenon arc lamp (LX300, Peccell Technologies, Inc.) served as a light source. Electrochemical impedance spectra (EIS) were recorded under an AC perturbation signal of 10 mV over the frequency range of 1 Hz to 100 kHz. The Mott-Schottky measurement was made at 1 kHz under dark conditions in 0.5 M Na₂SO₃.

Chapter 4: Results and Discussion

4.1. Photocatalytic H₂ production

4.1.1. Effect of the ratio of silica template to the precursor

The photocatalytic performance of the prepared samples was evaluated with H₂ production from water under visible-light irradiation, as shown in Figure 4-1. Experiments were done at three different ratios of the silica template to the precursor (3-amino 1, 2, 4-triazole), i.e. 0.5, 1 and 1.5. As it can be found from Figure 4-1, when the ratio is equal to 1, MCN has the highest activity. This could be related to pore-size distribution and surface area. Therefore, this optimum ratio of 1 was selected for the following experiments.

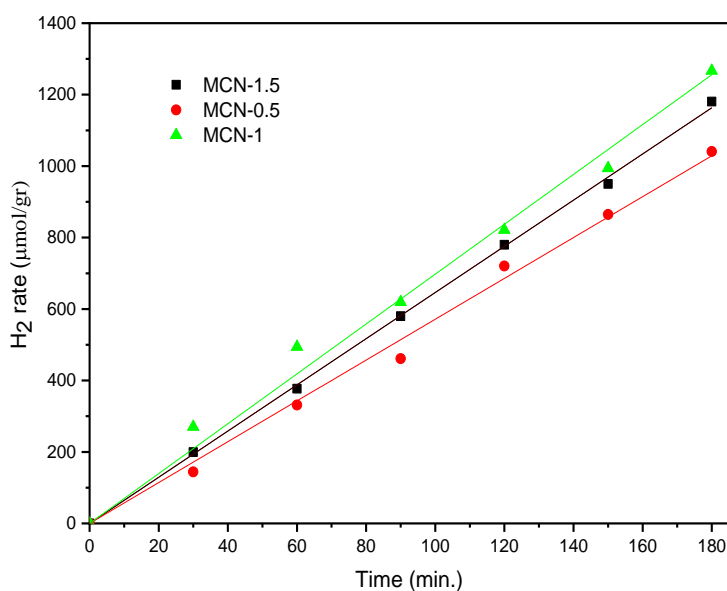


Figure 4-1. H₂ generation of MCN at different ratios of the silica template to the precursor. Reaction condition: 40 mg of catalyst in 40 mL of water/TEA solution (9:1 v/v) under visible light (≥ 420 nm)

4.1.2. Effect of the Co₃O₄ content on Co₃O₄/MCN

From Figure 4-2, it can be seen that after loading Co₃O₄ on the surface of MCN, all the Co₃O₄/MCN samples show higher photocatalytic activities than the bare MCN. The photocatalytic activity in H₂ evolution for Co₃O₄/MCN with 1.0, 3.0, 5.0, 7.0 and 10.0 wt% of Co₃O₄ content was recorded to be

1700, 2363, 2594, 1441 and 1327 $\mu\text{mol/g}$, respectively, which are all higher than that of the bare MCN (1267 $\mu\text{mol/g}$). This clearly shows that the photocatalyst activity of $\text{Co}_3\text{O}_4/\text{MCN}$ has been significantly improved compared to that of the bare MCN, which may be attributed to the enhanced visible-light harvesting and effective charge separation. The highest amount of hydrogen generation was reported at Co_3O_4 (5.0 wt%) /MCN, which was twice as high as the bare MCN. It is found that the photoactivity of $\text{Co}_3\text{O}_4/\text{MCN}$ decreases if the Co_3O_4 loaded content is larger than 5.0 wt%. This decline can be attributed to the loading of excessive Co_3O_4 leading to a decrease of the MCN surface active sites and relatively blockage of MCN pores.

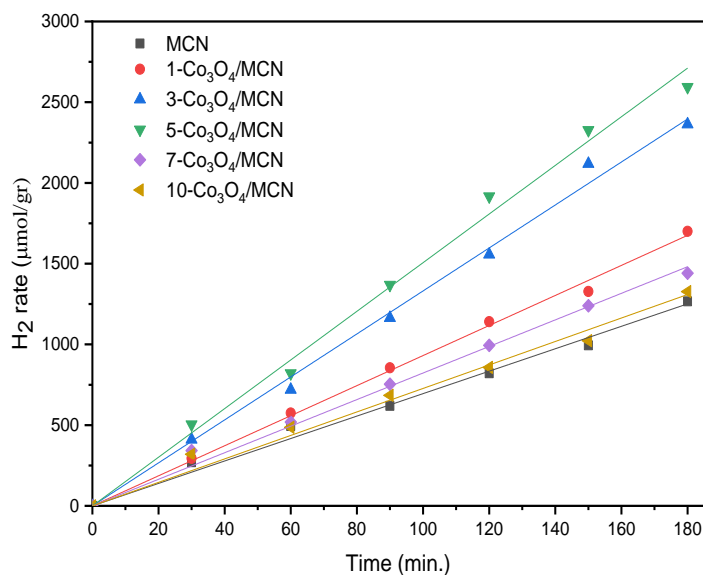


Figure 4-2. H_2 generation of MCN and $\text{Co}_3\text{O}_4/\text{MCN}$ at different contents of Co_3O_4 . Reaction condition: 40 mg of catalyst in 40 mL of water/TEA solution (9:1 v/v) under visible light (≥ 420 nm)

4.2. Material characterisation

4.2.1. XRD

X-ray diffraction (XRD) was conducted to investigate the crystal structures of MCN and $\text{Co}_3\text{O}_4/\text{MCN}$ with different contents of Co_3O_4 . As can be seen from Figure 4-3, the wide-angle XRD patterns of MCN reveal two XRD peaks at $2\theta = 13.2^\circ$ and 27.5° which could be indexed as the (002) and (100) planes of g- C_3N_4 (JCPDS 87-1526)⁶². These two diffraction peaks are in agreement with the bare MCN. A typical (002) peak around 27.5° was detected, which showed the graphite-like stacking of

the conjugated aromatic units of CN with a distance of 0.324 nm. The low angle diffraction peak of (100) that relates to a distance of 0.672 nm represents the in-plane structural packing motif of tris-triazine⁹⁷. For $\text{Co}_3\text{O}_4/\text{MCN}$ samples, the peaks at 18.9, 31.3, 36.9, 44.8, 55.6, 59.0 and 65.0° can be ascribed to the (111), (220), (311), (222), (400), (422), (511) and (440) planes of a face-centered cubic structure of Co_3O_4 , respectively (JCPDS no. 42-1467)⁹⁸. This shows the success of the Co_3O_4 deposition on MCN. Also, the intensities of the samples increased with an increase of the Co_3O_4 loading content.

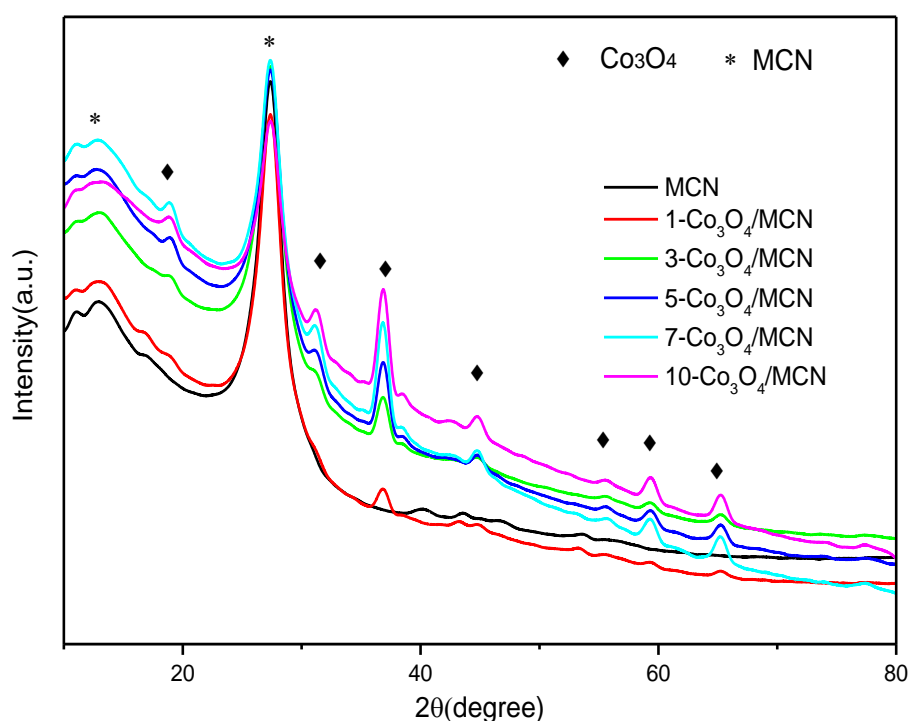


Figure 4-3. Wide-angle XRD patterns of MCN and $\text{Co}_3\text{O}_4/\text{MCN}$ with different contents of Co_3O_4 .

Figure 4-4 shows low-angle XRD pattern of MCN. The main peak (100) for MCN is observed at 0.74°. This pattern is feature of a mesoporous structure comprising short-ranged order in the pore arrangement⁹⁹.

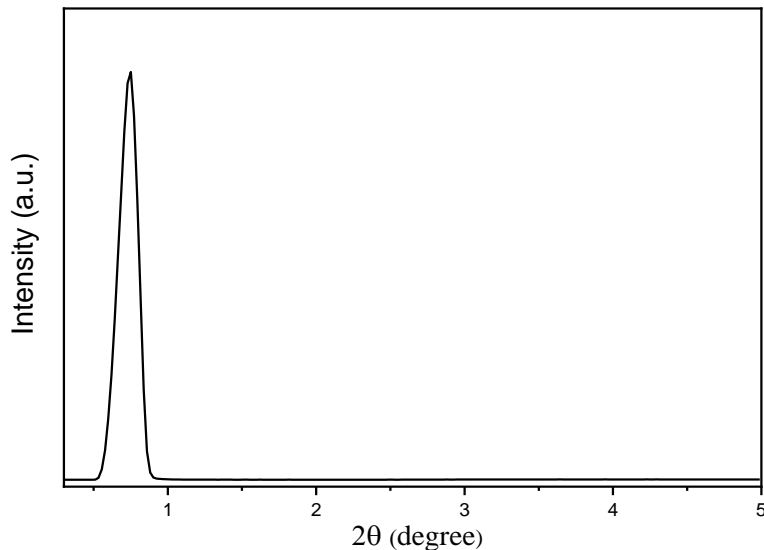


Figure 4-4. Low-angle XRD pattern of MCN.

4.2.2. FT-IR

The FT-IR spectra were recorded to study the chemical structure of the samples. Figure 4-5 shows FT-IR spectra of the MCN and $\text{Co}_3\text{O}_4/\text{MCN}$. For the bare MCN, several intense bands appear in the range from $1200\text{--}1700\text{ cm}^{-1}$, attributed to typical stretching vibration modes of the aromatic C-N (1238 , 1314 and 1405 cm^{-1}) and aromatic C=N stretching vibration (1562 and 1603 cm^{-1}). The sharp peak at 804 cm^{-1} is assigned to the breathing vibration of triazine units, presenting that the local structure of the obtained MCN is composed of triazine units. The broad peak at $2900\text{--}3500\text{ cm}^{-1}$ attributes to the stretching mode of N-H groups with an O-H vibration mode attached to the aromatic ring, derived from the surface uncondensed amine groups and the adsorbed water molecules. Also, the absence of the band around 2200 cm^{-1} confirms that there are no $\text{C}\equiv\text{N}$ bonds in the samples, reflecting the presence of a 1,3,5-triazine ring^{100,101}. After loading the Co_3O_4 with MCN, the main peaks of the MCN are maintained. For the $\text{Co}_3\text{O}_4/\text{MCN}$ samples, the peak at 658 cm^{-1} is associated with the ABO (A represents the Co^{2+} in a tetrahedral hole, B represents Co^{3+} in an octahedral hole and O represents oxygen) vibrations in the spinel lattice^{102,103}. With increasing the amount of Co_3O_4 into MCN structure, the intensity of this peak increased. As can be seen from Figure 4-5, this peak for 10- $\text{Co}_3\text{O}_4/\text{MCN}$ has the highest intensity. These results have agreement with the XRD results.

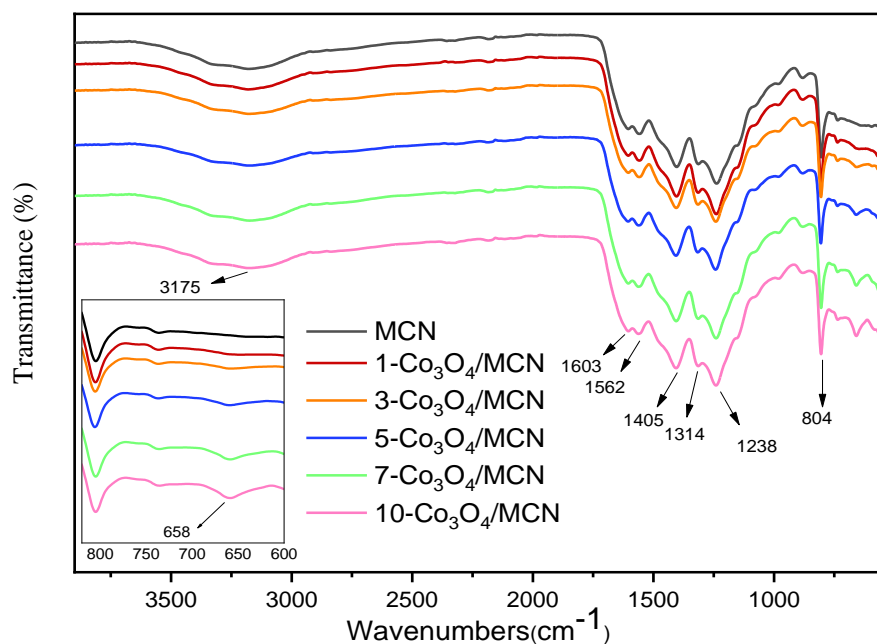


Figure 4-5. FTIR spectra of MCN and $\text{Co}_3\text{O}_4/\text{MCN}$ at different contents of Co_3O_4 .

4.2.3. BET

The surface area of the MCN materials could be controlled by varying the ratio of the silica template to the precursor. The nitrogen adsorption–desorption isotherms and Barrett–Joyner–Halenda (BJH) pore-size distributions depending on the desorption branch of the MCN samples at different ratios of the silica template to the precursor are shown in Figure 4-6. The isotherms of MCN samples display typical hysteresis with a type H3 hysteresis loop, showing the presence of mesopores, thereby indicating the successful generation of mesoporous structure in these samples according to the classification IUPAC, as indicated by Fig. 4-6. The values of the specific surface area, average pore diameters and pore volume of the samples at different ratios of the silica template to the precursor are summarized in Table 4-1. From figure 4-6(b) and Table 4-1, MCN samples have average pore diameters of 12–13 nm. Whereas the specific surface area of MCN-1 was the highest ($151.5 \text{ m}^2/\text{g}$), the surface area was low for MCN-0.5 and MCN-1.5 samples. The low surface area on MCN-0.5 could be the result of decreased formation of MCN because of the growth of CN without template confinement, which could occur when the mass ratio of the silica template to the precursor was too low. When the ratio of the silica template to the precursor was too high, surface area reduce which

could be related to framework collapse during silica washing due to the presence of extra amounts of silica. When other precursors such as urea and melamine were used, similar phenomenon has been reported according to literatures^{52,95}.

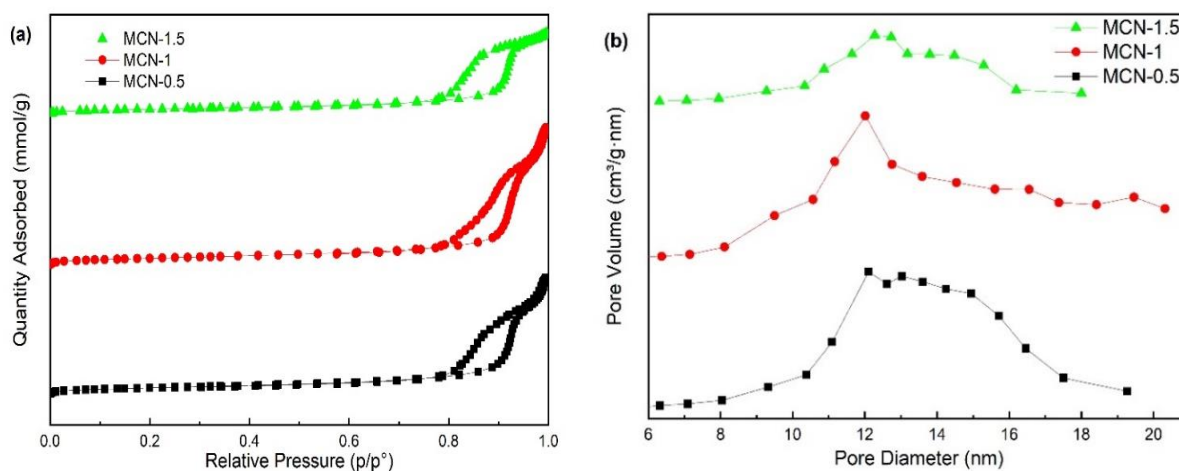


Figure 4-6. a) Nitrogen adsorption–desorption isotherms, b) Pore size distribution of MCN at different ratios of the silica template to the precursor

Table 4-1. Textural properties of MCN samples at different ratios of the silica template to the precursor

Samples	S_{BET}^a (m^2/g)	Pore volume^b (cm^3/g)	Average pore size (nm)
MCN-0.5	143.35	0.48	13.01
MCN-1	151.50	0.50	12.01
MCN-1.5	112.15	0.46	12.27

^a specific surface area was determined by the BET equation. ^b total pore volume was determined at $p/p_0=0.99$.

The nitrogen adsorption–desorption isotherms and BJH pore size distribution curves for MCN and Co_3O_4/MCN at different contents of Co_3O_4 are displayed in Figure 4-7. Each sample shows a typical type IV isotherm with H3 hysteresis loops at high partial pressures, regardless of Co_3O_4 loading amount, representing the presence of a mesoporous structure. The detailed textural properties of the MCN and Co_3O_4/MCN catalysts are summarized in Table 4-2. In addition, the BET surface areas increase with increasing the Co_3O_4 nanoparticles loading from 1 to 5 %; however, the BET surface areas gradually decrease with further increasing the Co_3O_4 nanoparticles loading to 7 % and 10 %.

This result suggests that MCN are partially blocked after excessive amount of Co_3O_4 nanoparticles is introduced. The pore size distribution curves clearly showed that all the samples distributed in the center of 12 nm, which is consistent with the size of the silica template, suggesting that the mesostructure is well-preserved. Additionally, after the introduction of Co_3O_4 , the pore size distribution of $\text{Co}_3\text{O}_4/\text{MCN}$ materials changed slightly, indicating that the mesoporosity of MCN remained intact.

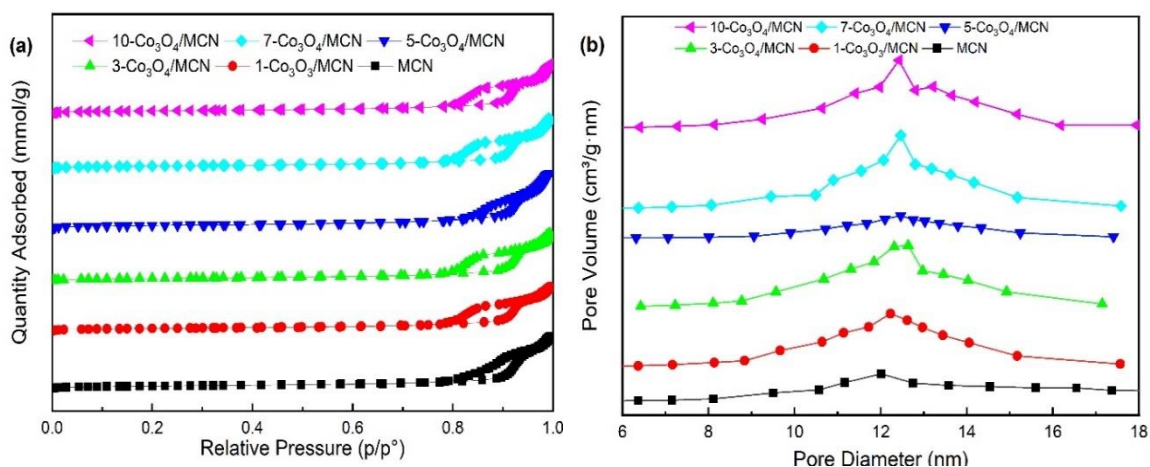


Figure 4-7. a) Nitrogen adsorption–desorption isotherms, b) Pore size distribution of MCN and $\text{Co}_3\text{O}_4/\text{MCN}$ at different contents of Co_3O_4 .

Table 4-2. Textural properties of MCN samples and $\text{Co}_3\text{O}_4/\text{MCN}$ at different contents of Co_3O_4 .

Samples	$S_{\text{BET}}^{\text{a}}$ (m^2/g)	Pore volume ^b (cm^3/g)	Average pore size (nm)
MCN	151.5	0.50	12.0
1- $\text{Co}_3\text{O}_4/\text{MCN}$	148.3	0.48	12.2
3- $\text{Co}_3\text{O}_4/\text{MCN}$	158.7	0.51	12.6
5- $\text{Co}_3\text{O}_4/\text{MCN}$	164.8	0.46	12.5
7- $\text{Co}_3\text{O}_4/\text{MCN}$	149.7	0.51	12.5
10- $\text{Co}_3\text{O}_4/\text{MCN}$	145.9	0.50	12.4

^a specific surface area was determined by the BET equation. ^b total pore volume was determined at $p/p_0=0.99$.

4.2.4. TEM and EDX

Morphologies for silica template, MCN and 5- $\text{Co}_3\text{O}_4/\text{MCN}$ samples were studied through TEM and the images are shown in Figure 4-8. MCN sample have mesosphere structures, which indicated the direct image of the silica templates that were removed using the ammonium hydrogen difluoride solution. These results have good agreement with the reported literatures on the structure of MCN even when using different precursor^{53,104}. The dark spherical spots corresponding to well-distributed Co_3O_4 nanoparticles in the surface of MCN are observed in Figure 4-8 (c).

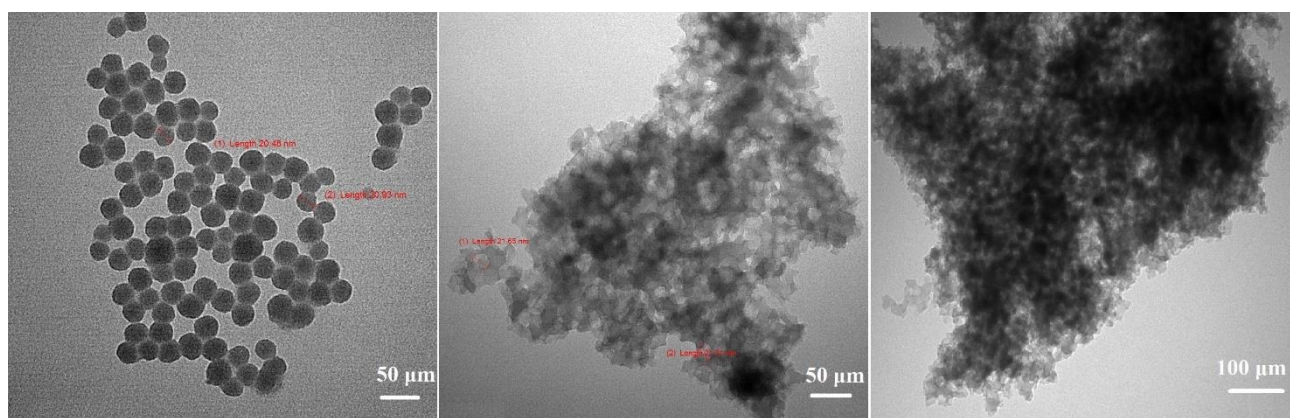


Figure 4-8. TEM images of silica template (a), MCN (b) and 5- $\text{Co}_3\text{O}_4/\text{MCN}$ (c) samples.

Figure 4-9 shows EDX analysis and corresponding elemental mapping of MCN and 5- $\text{Co}_3\text{O}_4/\text{MCN}$. Peaks for the elements C, N, O and Co are clearly seen in the EDX spectra. The EDX elemental mappings in Figure 4-9(b) indicate clearly that the cobalt element is distributed discretely on the MCN and no trace of agglomeration is found in the sample.

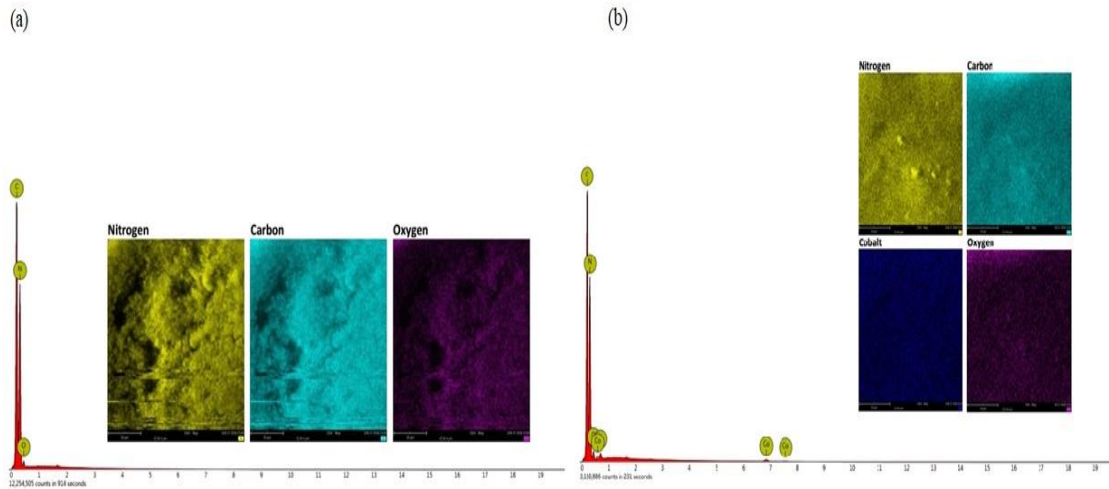


Figure 4-9. Energy dispersive X-ray (EDX) analysis and corresponding elemental mapping of N, C, O and Co elements in (a) MCN and (b) 5- $\text{Co}_3\text{O}_4/\text{MCN}$.

4.2.5. UV-vis diffuse reflectance spectra

As one of the most significant feature for photocatalyst, optical absorption was examined. UV-vis diffuse reflectance spectra of Co_3O_4 , MCN and 5- $\text{Co}_3\text{O}_4/\text{MCN}$ were shown in Figure 4-10 (a). The absorption edges are at about 639 nm and 667 nm for MCN and 5- $\text{Co}_3\text{O}_4/\text{MCN}$, respectively, which show shifted absorption edges for 5- $\text{Co}_3\text{O}_4/\text{MCN}$ in comparison with the bare MCN. Energy band gaps (E_g) of different samples can be calculated with the following equation¹⁰⁵:

$$\alpha h\nu = A(h\nu - E_g)^{\frac{n}{2}} \quad (4-1)$$

where α , A, h, E_g , ν are the absorption coefficient, constant, Planck's constant, the band gap energy and the incident light frequency, respectively. What is more, n depends on the transition type of semiconductor. $n = 1$ for direct transition, while n is 4 for indirect transition. Therefore, the values of Co_3O_4 , MCN and 5- $\text{Co}_3\text{O}_4/\text{MCN}$ are 1^{106,107}. Figure 4-10 (b) shows the band gap of Co_3O_4 , MCN and 5- $\text{Co}_3\text{O}_4/\text{MCN}$. The band gap of MCN is 2.2 eV which is very interesting result because this value is considerably lower than the band gap of g- C_3N_4 (2.7 eV) and other MCN reported in the literatures^{89,100}. The optical band gap is ascribed to the transitions between the weakly localized p-p*

states which originate from the sp^2 hybridization of C and N in the CN framework^{108,109}. The existence of clusters with or without lone pair states at p band produces a wider tail in the absorption spectrum and the band gap drops to 2.20 eV⁵⁵. For 5- $\text{Co}_3\text{O}_4/\text{MCN}$, the band gap decreased to 2.1 eV showing the improved light harvesting ability and providing more charge carriers upon illumination than MCN which lead to higher photocatalytic activity.

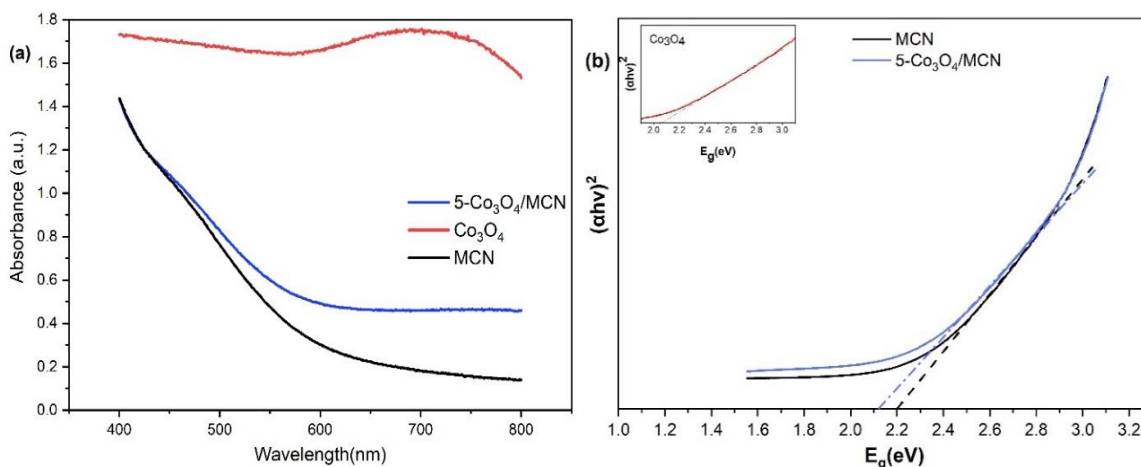


Figure 4-10. a) UV-vis diffuse reflectance spectra, b) Tauc plots of Co_3O_4 , MCN and 5- $\text{Co}_3\text{O}_4/\text{MCN}$

4.2.6. Photoluminescence

Photoluminescence (PL) analysis is a useful tool to study the migration, transfer and the separation of photogenerated electrons and holes in the semiconductors, since PL emission of semiconductor results from the charge carrier recombination^{110,111}. The sharp intensity of PL spectra depends upon the rate of recombination of photogenerated excitons. It is commonly known that a lower PL emission intensity links to a lower carrier recombination rate^{112,113}. Figure 4-11 displays the PL spectra of MCN and 5- $\text{Co}_3\text{O}_4/\text{MCN}$ at the excitation wavelength of 330 nm at room temperature. The MCN has a strong emission peak at around 490 nm. The emission intensity of 5- $\text{Co}_3\text{O}_4/\text{MCN}$ sample is lower than that of pristine g- C_3N_4 at the similar emission position, indicating that electron-pairs recombination of 5- $\text{Co}_3\text{O}_4/\text{MCN}$ is suppressed. The above result proposes that effective separation, transportation, and capture of the photogenerated carriers were obtained after loading Co_3O_4 on MCN structure, further favouring the improved H_2 generation.

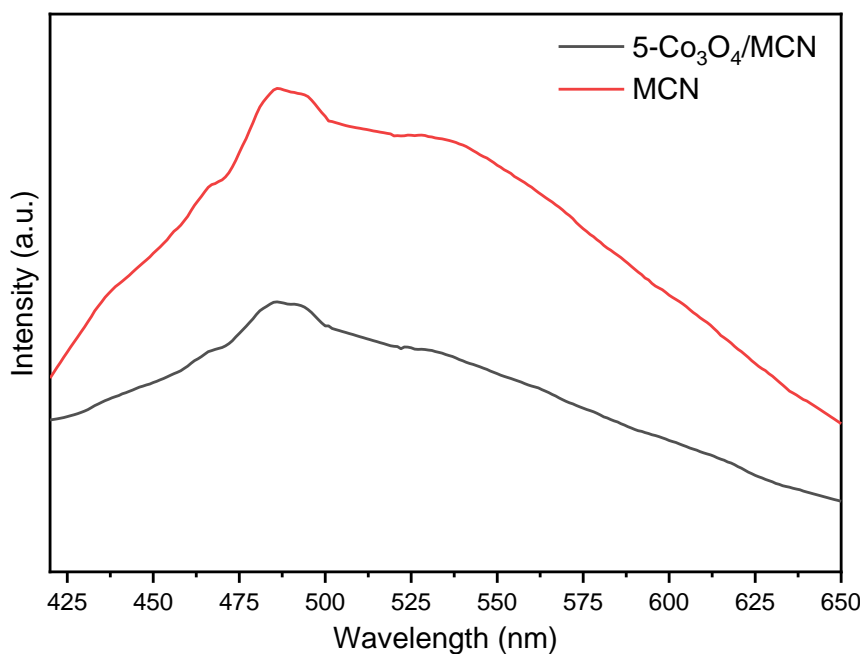


Figure 4-11. PL spectra of the MCN and 5-Co₃O₄/MCN

4.2.7. Transient photocurrent responses

For photocatalyst applications, electron-hole separation character is crucially important. Transient photocurrent analysis is a broadly used technique to investigate the electron-hole separation effect. Photocurrent could directly show the mobility capability of the photogenerated electrons, and the higher peak intensity means the higher separation of the photogenerated carriers,¹¹⁴ which has a positive correlation with the photocatalytic activity of the photocatalyst directly¹¹⁵. The fast and reproducible photocurrent response for several on-off cycles of visible light irradiation (≥ 420 nm) is shown in Figure 4-12. The photocurrent value increases rapidly at a maximum value when the light turned on due to the separation of electron hole pairs at the heterostructure-electrolyte interface. On the contrary, when turning off the light, the photocurrent rapidly decreased to the initial condition. Since recombination rate of electrons and holes of bare MCN electrode is high, this electrode displays relative weak photocurrent. After loading Co₃O₄ on MCN, the resulted electrode shows stable which is 1.45 times higher photocurrent than the bare MCN electrode, indicating that the loaded Co₃O₄ can efficiently trap photogenerated electrons of excited MCN and transfer these electrons to the back contact. Therefore, an efficient charge separation could be obtained, allowing more charge carriers to

take part in photocatalytic H₂ production reaction. Furthermore, its reproducibility and stability are excellent as the illumination was turned on and off.

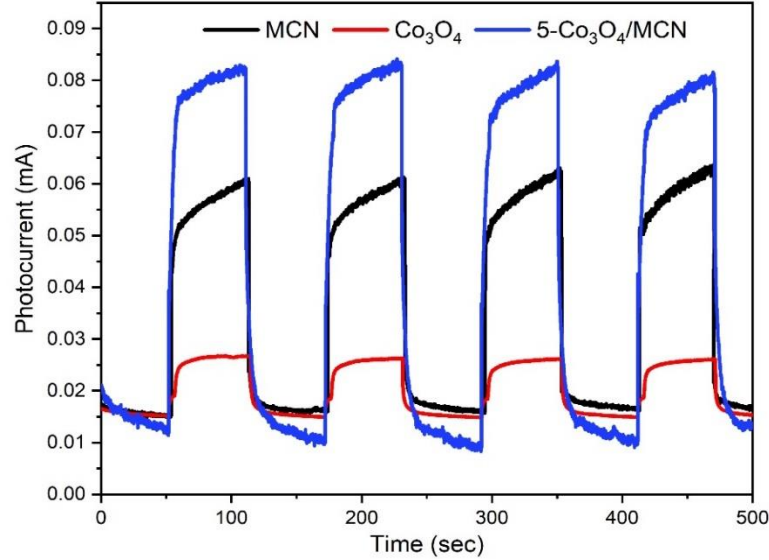


Figure 4-12. Photocurrent responses under visible-light irradiation with 60 s light on-off cycles of the Co₃O₄, MCN and 5-Co₃O₄/MCN

4.2.8. Mott-Schottky

Figure 4-13 presents the Mott-Schottky plots of the MCN and Co₃O₄, in which C^{-2} is plotted against the applied potential. The positive slope of the plot related to MCN reveals the n-type semiconductor material. Herein, the flat band potential of the electrodes was obtained by the Mott-Schottky relation defined as follows:

$$C^{-2} = \frac{2}{e\epsilon\epsilon_0 N_d} \left(V_a - V_{fb} - \frac{kT}{e} \right) \quad (4-2)$$

where k is Boltzmann's constant, C is the space charge layer capacitance, ϵ is the dielectric constant, e is the electron charge, ϵ_0 is the vacuum permittivity, V_a is the applied potential, N_d is the donor density of electron, T is the Kelvin temperature of operation, and V_{fb} is the flat band potential. The flat band potential (V_{fb}) was determined by taking the x intercept of a linear fit to the Mott-Schottky plot, C^{-2} as a function of applied potential (V_a), and calculated from the following equation:

$$V_{int} = V_{fb} + \frac{kT}{e} \quad (4-3)$$

The conduction band potential (E_{CB}) of the n-type semiconductor is assumed to be 0.1 V more negative than E_{fb} ¹¹⁶. Based on the V_{int} values shown in Figure 4-9, the flat band potential value is estimated to be -1.02 V vs. Ag/AgCl (considering $\frac{kT}{e}=0.02$ V) which is equivalent to -0.82 V vs. NHE. As a result, E_{CB} of MCN is around -0.92 V. The Mott-Schottky plot of Co_3O_4 shows p-type characteristics (Figure 4-13 (b)). The flat band potential is 1.48 V vs. Ag/AgCl (calculated from (1) and (2) equations), which is equivalent to 1.68 V vs. NHE. For p-type semiconductor, the flat band potential is equal to the valence band potential¹¹⁷.

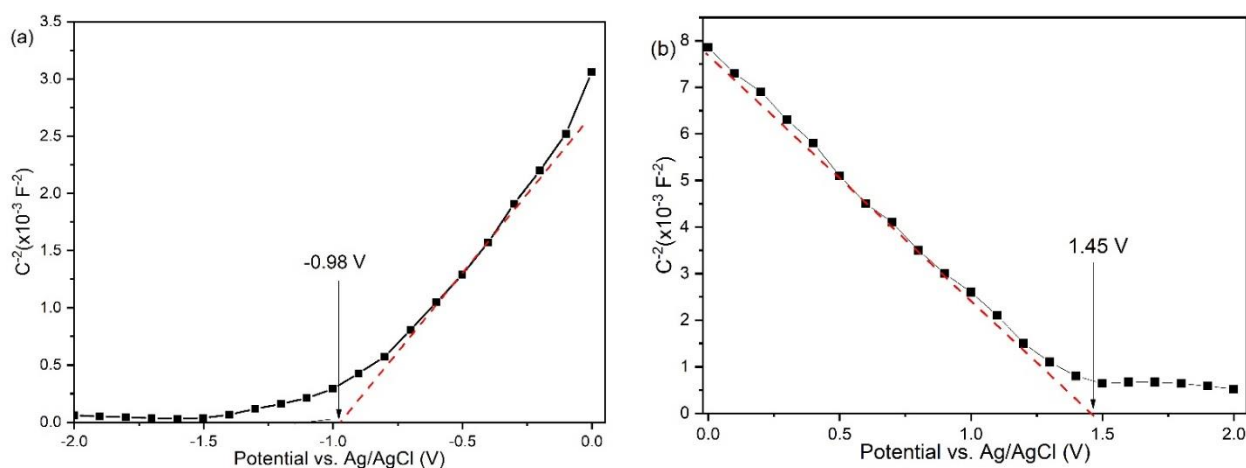


Figure 4-13. Mott-Schottky plots of a) MCN and b) Co_3O_4

4.2.9. Electrochemical impedance spectroscopy

The charge transport resistance was analyzed by electrochemical impedance spectroscopy (EIS). The EIS plots of MCN and 5- Co_3O_4 /MCN are shown in Figure 4-14. The diameter of semicircle means the charge transfer resistance at high frequencies for each Nyquist plot. The smaller the semicircle diameter, the smaller the charge transfer resistance and hence the higher the charge transfer and separation efficiency and the higher the electrical conductivity of the materials. It can be seen that the arcs of both MCN and 5- Co_3O_4 /MCN are very big in dark. While under the visible light irradiation, the diameter of semicircles is much smaller than those in dark. This could be ascribed to the presence of electrons and holes induced by incident light. In both cases, the decrease of semicircle diameter

shows that by loading Co_3O_4 on MCN, the offered resistance for the charge transportation is reduced remarkably.

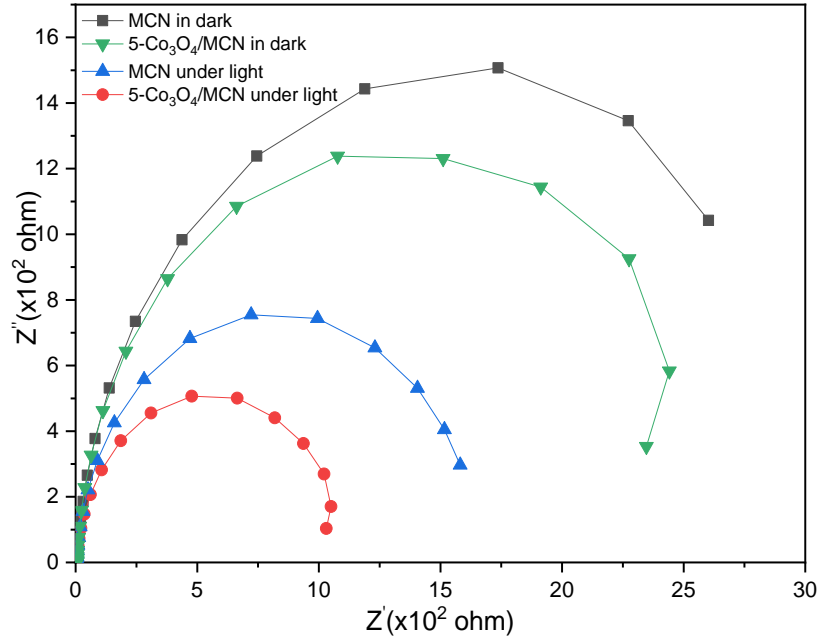


Figure 4-14. EIS of MCN and 5- Co_3O_4 /MCN both in dark and under light.

4.3. Photocatalytic mechanism

It is well known that the enhancement of photocatalytic performance of composite photocatalysts is mainly attributed to electrons and holes transfer at the interfaces of photocatalysts¹¹⁸. Structural properties and band structure of a photocatalyst is the foundation for exploring its photocatalytic mechanism. Based on the CB and VB energy levels, the electron and hole transfer will take place. Three methods to calculate the band edge positions are existence: experiments according to photoelectrochemical techniques, theoretical calculation based on the first principle, and calculating theoretically from the absolute (or Mulliken) electronegativity^{119,120,121}. The third one is a simple method with sensible results for many oxides photocatalysts^{122,123}. The theoretical band positions of VB and CB for the MCN and Co_3O_4 can be calculated by using the empirical equations as follows¹²⁴:

$$E_{VB} = \chi - E^e + 1/2E_g \quad (4-4)$$

$$E_{CB} = E_{VB} - E_g \quad (4-5)$$

Where E_{CB} is the CB edge potential, and X is the absolute electronegativity of the semiconductor. E° is the energy of the free electrons on the hydrogen scale, approximately 4.5 eV. E_g is the bandgap of the semiconductor which obtains from Tauc plot based on UV-vis result. Finally, χ is defined as the geometric mean of the absolute electronegativity of the constituent atoms, and it was calculated using the following equation:

$$\chi = [(A)^a \times (B)^b \times (C)^c]^{\frac{1}{a+b+c}} \quad (4-6)$$

In which a, b, and c are the number of atoms in the compounds and A, B and C are defined as an absolute electronegativity of the constituent atoms, which is defined as the arithmetic mean of the atomic electron affinity and the first ionization energy. χ values for Co_3O_4 and MCN are 5.90 and 4.64 respectively^{125, 126}. From the above formula, the E_{VB} and E_{CB} values of both semiconductors are estimated and shown in Table 4-3.

Table 4-3. The absolute electronegativity, band gap energy, valence, and conduction band edges of MCN and Co_3O_4 based on a theoretical formula

Semiconductor	Absolute electronegativity (χ)	Band gap energy (eV)	Valence band potential E_{VB} (eV)	Conduction band potential E_{CB} (eV)
MCN	4.64	2.2	1.24	- 0.96
Co_3O_4	5.90	2.06	2.43	0.37

Based on the Mott-Schottky results and band gap formula, CB and VB of MCN and Co_3O_4 were also calculated. Figure 4-15 showed the difference between CB and VB values based on theoretical and experimental results.

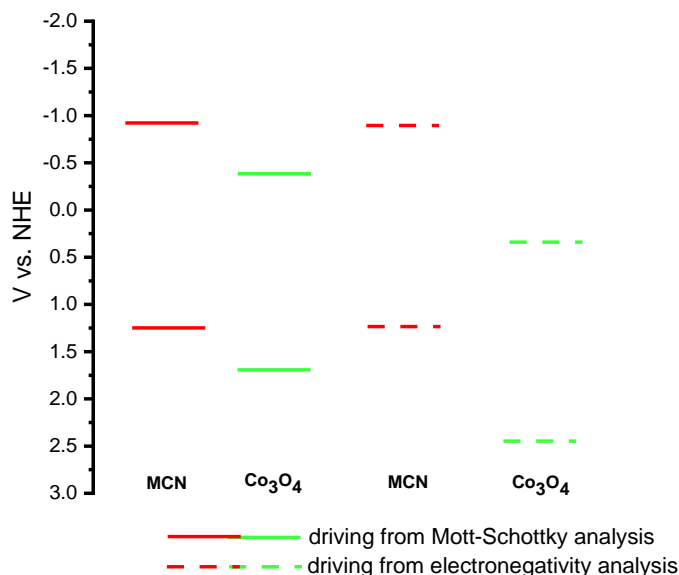


Figure 4-15. Schematic band structures of MCN and Co₃O₄ obtaining from Mott-Schottky and electronegativity analysis

In fact, CB and VB values obtained from theoretical measurement are slightly different than the experimental value, but this does not affect the comparison of their relative positions. On the basis of the above results including photocurrent measurements, PL spectra, EIS, and photocatalytic activity results, a possible mechanism of photocatalytic H₂ evolution using the composite photocatalysts is proposed and illustrated in Figure 4-16. It is well-known that p-n heterojunction composite photocatalysts with appropriate energy band positions are very favorable for photocatalysis with sufficient efficiency. Among few p-type semiconductors, Co₃O₄ can easily form p-n heterojunction composites. With the induction of light, both MCN and Co₃O₄ can produce photogenerated electron-hole pairs. Co₃O₄ as a p-type semiconductor, which always shows good stability under illumination, and MCN is defined as an n-type semiconductor. Thus, a p-n heterojunction would be formed at the interfaces of Co₃O₄ loaded MCN composite. As illustrated in Figure 4-15, the Co₃O₄ and MCN photocatalysts possess matchable band energy levels. Then, an effective heterojunction structure between Co₃O₄ and MCN can be fabricated. Since CB of MCN is located at -0.92 eV which is negative than CB of Co₃O₄, photogenerated electrons in CB of the MCN could easily transfer to the CB of Co₃O₄. The photoinduced holes in the VB of Co₃O₄ will migrate to the VB of MCN according to the

traditional electron-hole separation process^{127,128}. As a result, Co_3O_4 particles serve as an effective electron acceptor, and MCN serve as effective hole acceptor, which is beneficial for simplifying the separation of the photogenerated carriers, which greatly inhibits the recombination of photogenerated electrons and holes, leading to increased photocatalytic performance which has agreement with the result illustrated for H_2 production in section 4.1 (Figure 4.2).

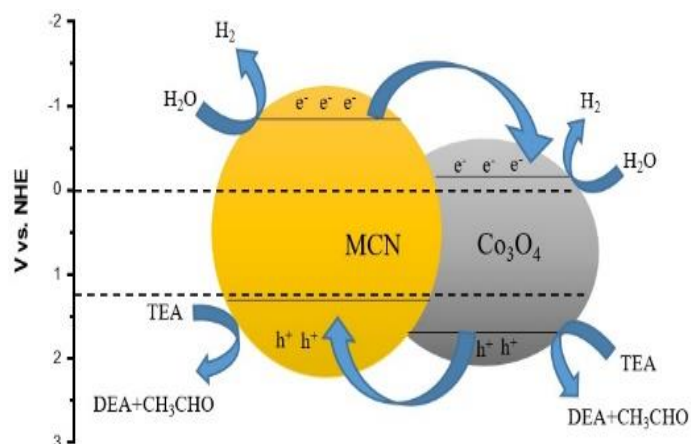


Figure 4.16 Schematic illustration of the photocatalytic mechanism.

Chapter 5: Conclusions and Future Work

5.1. Concluding comments

The goal of the research described in this thesis has been to design MCN and $\text{Co}_3\text{O}_4/\text{MCN}$ for hydrogen generation under visible light irradiation. MCN was synthesised via hard template using 3-amino 1, 2, 4-triazole and SiO_2 nanoparticles as a precursor and silica template, respectively. MCN shows high activity without using any co-catalyst. To increase the activity of the catalyst and its properties, Co_3O_4 was loaded on MCN structure via impregnation method. The following are the significant contributions of this research:

- Effect of ratio of the silica template to precursor on photocatalytic performance: when this ratio is equal to one, we have the highest activity which could be related to the higher surface area.
- Effect of weight percentage of Co_3O_4 : Co_3O_4 was loading on MCN at different percentages. With increasing Co_3O_4 amount up to 5%, activity increased and after that decreased which could be the decrease of the MCN surface active sites and relatively blockage of MCN pores. Photocatalyst activity at 5 % was twice as high as the bare MCN.
- XRD test showed the success of MCN synthesis and the Co_3O_4 deposition on MCN.
- FT-IR test characterized the MCN and $\text{Co}_3\text{O}_4/\text{MCN}$ structure and confirmed the presence of triazine ring, NH_2 and NH groups in MCN and also confirmed the loading Co_3O_4 on MCN
- BET measurement displays mesoporous structure and high surface area for MCN and $\text{Co}_3\text{O}_4/\text{MCN}$.
- TEM and EDX results showed the formation of mesoporous structure and showed that the Co nanoparticles were uniformly dispersed and not agglomerated on the surface of the MCN.
- UV-visible results show that narrow band gap of around 2.2 eV for MCN and $\text{Co}_3\text{O}_4/\text{MCN}$ are determined, showing better light harvesting ability in comparison with MCN.
- Photoluminescence, photocurrent, and electrochemical impedance spectroscopy results indicate that the charge transfer and the photogenerated electrons and holes separation efficiently increase after loading Co_3O_4 on MCN structure.

- Photocatalytic mechanism is proposed based on the results. The p-n heterojunction was fabricated which leads to the easily photogenerated carriers separation and suppress the recombination rate and consequently improving photocatalytic performance

5.2. Future work

A series of ideas that could be further carried out for this project is proposed in this section. To obtain the amount of carbon and nitrogen in MCN structure, CNH analyser is required. Also, getting XPS analysis could be helpful to understand the chemical state of elements. Since SiO₂ nanoparticles were used as a silica template in this project, using other silica templates such as KIT-6 and SBA-15 can be used and compared with the result of this project regarding photocatalyst performance. Another parameter which could affect photocatalyst performance is a precursor. 3-amino 1, 2, 4-triazole was used as a precursor in this project. Others precursors like melamine, cyanamide can be used for the fabrication of MCN and compare the activity with MCN which fabricate from 3-amino 1, 2, 4-triazole.

References:

- (1) Surroop, D.; Raghoo, P. Energy Landscape in Mauritius. *Renew. Sustain. Energy Rev.* **2017**, *73* (January), 688–694.
- (2) Moniz, S. J. A.; Shevlin, S. A.; Martin, D. J.; Guo, Z.-X.; Tang, J. Visible-Light Driven Heterojunction Photocatalysts for Water Splitting - a Critical Review. *Energy Environ. Sci.* **2015**, *8* (3), 731–759.
- (3) Acar, C.; Dincer, I.; Naterer, G. F. Review of Photocatalytic Water-Splitting Methods for Sustainable Hydrogen Production. **2016**, No. May, 1449–1473.
- (4) FUJISHIMA, A.; HONDA, K. Electrochemical Photolysis of Water at a Semiconductor Electrode. *Nature* **1972**, *238*, 37.
- (5) Demeestere, K.; Dewulf, J.; Van Langenhove, H. Heterogeneous Photocatalysis as an Advanced Oxidation Process for the Abatement of Chlorinated, Monocyclic Aromatic and Sulfurous Volatile Organic Compounds in Air: State of the Art. *Crit. Rev. Environ. Sci. Technol.* **2007**, *37* (6), 489–538.
- (6) Kudo, A.; Miseki, Y. Heterogeneous Photocatalyst Materials for Water Splitting. *Chem. Soc. Rev.* **2009**, *38* (1), 253–278.
- (7) Abe, R. Recent Progress on Photocatalytic and Photoelectrochemical Water Splitting under Visible Light Irradiation. *J. Photochem. Photobiol. C Photochem. Rev.* **2010**, *11* (4), 179–209.
- (8) Linsebigler, A. L.; Lu, G.; Yates, J. T. Photocatalysis on TiO₂ Surfaces: Principles, Mechanisms, and Selected Results. *Chem. Rev.* **1995**, *95* (3), 735–758.
- (9) Yang, J.; Wang, D.; Han, H.; Li, C. Roles of Cocatalysts in Photocatalysis and Photoelectrocatalysis. *Acc. Chem. Res.* **2013**, *46* (8), 1900–1909.
- (10) Ahmed, A. Y.; Kandiel, T. A.; Ivanova, I.; Bahnemann, D. Photocatalytic and Photoelectrochemical Oxidation Mechanisms of Methanol on TiO₂ in Aqueous Solution. *Appl. Surf. Sci.* **2014**, *319*, 44–49.
- (11) Serpone, N.; Emeline, A. V. Semiconductor Photocatalysis — Past, Present, and Future Outlook. *J. Phys. Chem. Lett.* **2012**, *3* (5), 673–677.
- (12) Roland, M. Photocatalysis: Semiconductor Composites: Strategies for Enhancing Charge Carrier Separation to Improve Photocatalytic Activity (Adv. Funct. Mater. 17/2014). *Adv. Funct. Mater.* **2014**, *24* (17), 2420.
- (13) Chen, C.; Ma, W.; Zhao, J. Semiconductor-Mediated Photodegradation of Pollutants under Visible-Light Irradiation. *Chem. Soc. Rev.* **2010**, *39* (11), 4206–4219.
- (14) Hernandez-Alonso, M. D.; Fresno, F.; Suarez, S.; Coronado, J. M. Development of Alternative Photocatalysts to TiO₂: Challenges and Opportunities. *Energy Environ. Sci.* **2009**, *2* (12), 1231–1257.

- (15) Carp, O.; Huisman, C. L.; Reller, A. Photoinduced Reactivity of Titanium Dioxide. *Prog. Solid State Chem.* **2004**, *32* (1), 33–177.
- (16) Petkovich, N. D.; Stein, A. Controlling Macro- and Mesopores with Hierarchical Porosity through Combined Hard and Soft Templating. *Chem. Soc. Rev.* **2013**, *42* (9), 3721–3739.
- (17) Li, W.; Wu, Z.; Wang, J.; Elzatahry, A. A.; Zhao, D. A Perspective on Mesoporous TiO₂ Materials. *Chem. Mater.* **2014**, *26* (1), 287–298.
- (18) Ismail, A. A. Mesoporous PdO–TiO₂ Nanocomposites with Enhanced Photocatalytic Activity. *Appl. Catal. B Environ.* **2012**, *117–118*, 67–72.
- (19) Park, H.; Park, Y.; Kim, W.; Choi, W. Surface Modification of TiO₂ Photocatalyst for Environmental Applications. *J. Photochem. Photobiol. C Photochem. Rev.* **2013**, *15*, 1–20.
- (20) Ahmad, H.; Kamarudin, S. K.; Minggu, L. J.; Kassim, M. Hydrogen from Photo-Catalytic Water Splitting Process: A Review. *Renew. Sustain. Energy Rev.* **2015**, *43*, 599–610.
- (21) Yu, J.; Zhou, P.; Li, Q. New Insight into the Enhanced Visible-Light Photocatalytic Activities of B-, C- and B/C-Doped Anatase TiO₂ by First-Principles. *Phys. Chem. Chem. Phys.* **2013**, *15* (29), 12040–12047.
- (22) Mishra, M.; Chun, D.-M. α -Fe₂O₃ as a Photocatalytic Material: A Review. *Appl. Catal. A Gen.* **2015**, *498*, 126–141.
- (23) Chen, X.; Wu, Z.; Liu, D.; Gao, Z. Preparation of ZnO Photocatalyst for the Efficient and Rapid Photocatalytic Degradation of Azo Dyes. *Nanoscale Res. Lett.* **2017**, *12* (1), 143.
- (24) Ma, Y.; Zhao, X.; Niu, M.; Li, W.; Wang, X.; Zhai, C.; Wang, T.; Tang, Y.; Dai, X. Monoclinic Ga₂O₃ (100) Surface as a Robust Photocatalyst for Water-Splitting. *RSC Adv.* **2017**, *7* (7), 4124–4134.
- (25) Chua, C. S.; Ansovini, D.; Lee, C. J. J.; Teng, Y. T.; Ong, L. T.; Chi, D.; Hor, T. S. A.; Raja, R.; Lim, Y.-F. The Effect of Crystallinity on Photocatalytic Performance of Co₃O₄ Water-Splitting Cocatalysts. *Phys. Chem. Chem. Phys.* **2016**, *18* (7), 5172–5178.
- (26) Kong, L.; Chen, H.; Hua, W.; Zhang, S.; Chen, J. Mesoporous Bismuth Titanate with Visible-Light Photocatalytic Activity. *Chem. Commun.* **2008**, No. 40, 4977–4979.
- (27) Hosogi, Y.; Shimodaira, Y.; Kato, H.; Kobayashi, H.; Kudo, A. Role of Sn²⁺ in the Band Structure of SnM₂O₆ and Sn₂M₂O₇ (M = Nb and Ta) and Their Photocatalytic Properties. *Chem. Mater.* **2008**, *20* (4), 1299–1307.
- (28) Walsh, A.; Yan, Y.; Huda, M. N.; Al-Jassim, M. M.; Wei, S.-H. Band Edge Electronic Structure of BiVO₄: Elucidating the Role of the Bi s and V d Orbitals. *Chem. Mater.* **2009**, *21* (3), 547–551.
- (29) Ismail, A. A.; Bahnemann, D. W. Photochemical Splitting of Water for Hydrogen Production by Photocatalysis: A Review. *Sol. Energy Mater. Sol. Cells* **2014**, *128*, 85–101.
- (30) Kenneth, J. *Nanoscale Materials in Chemistry*; 2009.

References

- (31) Ma, Z. Cobalt Oxide Catalysts for Environmental Remediation. *Curr. Catal.* **2014**, *3* (1), 15–26.
- (32) Mate, V. R.; Shirai, M.; Rode, C. V. Heterogeneous Co₃O₄ Catalyst for Selective Oxidation of Aqueous Veratryl Alcohol Using Molecular Oxygen. *Catal. Commun.* **2013**, *33*, 66–69.
- (33) Wu, R.-J.; Wu, J.-G.; Yu, M.-R.; Tsai, T.-K.; Yeh, C.-T. Promotive Effect of CNT on Co₃O₄–SnO₂ in a Semiconductor-Type CO Sensor Working at Room Temperature. *Sensors Actuators B Chem.* **2008**, *131* (1), 306–312.
- (34) Electrodynamic, C. Electrochromic Properties of Cobalt Oxide Thin Films Prepared by Chemical Vapor Deposition. **1996**, *143* (4), 1993–1996.
- (35) Du, N.; Zhang, H.; Chen, B. D.; Wu, J. B.; Ma, X. Y.; Liu, Z. H.; Zhang, Y. Q.; Yang, D. R.; Huang, X. H.; Tu, J. P. Porous Co₃O₄ Nanotubes Derived From Co₄(CO)₁₂ Clusters on Carbon Nanotube Templates: A Highly Efficient Material For Li-Battery Applications. *Adv. Mater.* **2007**, *19* (24), 4505–4509.
- (36) Wang, R. M.; Liu, C. M.; Zhang, H. Z.; Chen, C. P.; Guo, L.; Xu, H. B.; Yang, S. H. Porous Nanotubes of Co₃O₄: Synthesis, Characterization, and Magnetic Properties. *Appl. Phys. Lett.* **2004**, *85* (11), 2080–2082.
- (37) Lou, X.; Han, J.; Chu, W.; Wang, X.; Cheng, Q. Synthesis and Photocatalytic Property of Co₃O₄ Nanorods. *Mater. Sci. Eng. B* **2007**, *137* (1), 268–271.
- (38) Chen, J.; Wu, X.; Selloni, A. Electronic Structure and Bonding Properties of Cobalt Oxide in the Spinel Structure. *Phys. Rev. B* **2011**, *83* (24), 245204.
- (39) Rahman, M. Z.; Davey, K.; Qiao, S.-Z. Carbon, Nitrogen and Phosphorus Containing Metal-Free Photocatalysts for Hydrogen Production: Progress and Challenges. *J. Mater. Chem. A* **2018**, *6* (4), 1305–1322.
- (40) M., M. B. C.; M., H. G. A.; A., C. C.; Sebastian, P.; Robert, G.; R., D. J.; Erwin, R. Enhancing Light Absorption and Charge Transfer Efficiency in Carbon Dots through Graphitization and Core Nitrogen Doping. *Angew. Chemie Int. Ed.* **2017**, *56* (23), 6459–6463.
- (41) Murakami, N.; Tango, Y.; Miyake, H.; Tajima, T.; Nishina, Y.; Kurashige, W.; Negishi, Y.; Takaguchi, Y. SWCNT Photocatalyst for Hydrogen Production from Water upon Photoexcitation of (8, 3) SWCNT at 680-Nm Light. *Sci. Rep.* **2017**, *7*, 43445.
- (42) Yeh, T.-F.; Cihlář, J.; Chang, C.-Y.; Cheng, C.; Teng, H. Roles of Graphene Oxide in Photocatalytic Water Splitting. *Mater. Today* **2013**, *16* (3), 78–84.
- (43) Jelinek, R. *Carbon Quantum Dots Synthesis, Properties and Applications*; 2016.
- (44) Han, M.; Zhu, S.; Lu, S.; Song, Y.; Feng, T.; Tao, S.; Liu, J.; Yang, B. Recent Progress on the Photocatalysis of Carbon Dots: Classification, Mechanism and Applications. *Nano Today* **2018**, *19*, 201–218.
- (45) A., T. The Role of Carbon Nanotubes in Enhancement of Photocatalysis. In *Syntheses and*

Applications of Carbon Nanotubes and Their Composites; 2013.

- (46) Sohail, M.; Saleem, M.; Ullah, S.; Saeed, N.; Afridi, A.; Khan, M.; Arif, M. Modified and Improved Hummer's Synthesis of Graphene Oxide for Capacitors Applications. *Mod. Electron. Mater.* **2017**, *3* (3), 110–116.
- (47) Hatakeyama, K.; Tateishi, H.; Taniguchi, T.; Koinuma, M.; Kida, T.; Hayami, S.; Yokoi, H.; Matsumoto, Y. Tunable Graphene Oxide Proton/Electron Mixed Conductor That Functions at Room Temperature. *Chem. Mater.* **2014**, *26* (19), 5598–5604.
- (48) Zhang, N.; Zhang, Y.; Xu, Y.-J. Recent Progress on Graphene-Based Photocatalysts: Current Status and Future Perspectives. *Nanoscale* **2012**, *4* (19), 5792.
- (49) Han, L.; Wang, P.; Dong, S. Progress in Graphene-Based Photoactive Nanocomposites as a Promising Class of Photocatalyst. *Nanoscale* **2012**, *4* (19), 5814–5825.
- (50) Wang, X.; Maeda, K.; Thomas, A.; Takahane, K.; Xin, G.; Carlsson, J. M.; Domen, K.; Antonietti, M. A Metal-Free Polymeric Photocatalyst for Hydrogen Production from Water under Visible Light. *Nat. Mater.* **2008**, *8*, 76.
- (51) Li, H.; Wang, L.; Liu, Y.; Lei, J.; Zhang, J. Mesoporous Graphitic Carbon Nitride Materials: Synthesis and Modifications. *Res. Chem. Intermed.* **2016**, *42* (5), 3979–3998.
- (52) Lee, S. C.; Lintang, H. O.; Yuliati, L. A Urea Precursor to Synthesize Carbon Nitride with Mesoporosity for Enhanced Activity in the Photocatalytic Removal of Phenol. *Chem. - An Asian J.* **2012**, *7* (9), 2139–2144.
- (53) Goettmann, F.; Fischer, A.; Antonietti, M.; Thomas, A. Chemical Synthesis of Mesoporous Carbon Nitrides Using Hard Templates and Their Use as a Metal-Free Catalyst for Friedel-Crafts Reaction of Benzene. *Angew. Chemie - Int. Ed.* **2006**, *45* (27), 4467–4471.
- (54) Zhai, H.-S.; Cao, L.; Xia, X.-H. Synthesis of Graphitic Carbon Nitride through Pyrolysis of Melamine and Its Electrocatalysis for Oxygen Reduction Reaction. *Chinese Chem. Lett.* **2013**, *24* (2), 103–106.
- (55) P., M. G.; N., T. S.; S., L. K.; Hamid, I.; Ugo, R.; Khalid, A.; Toshiyuki, M.; Dae-Hwan, P.; Ajayan, V. Highly Ordered Nitrogen-Rich Mesoporous Carbon Nitrides and Their Superior Performance for Sensing and Photocatalytic Hydrogen Generation. *Angew. Chemie Int. Ed.* **2017**, *56* (29), 8481–8485.
- (56) Lakhi, K. S.; Park, D.-H.; Al-Bahily, K.; Cha, W.; Viswanathan, B.; Choy, J.-H.; Vinu, A. Mesoporous Carbon Nitrides: Synthesis, Functionalization, and Applications. *Chem. Soc. Rev.* **2017**, *46* (1), 72–101.
- (57) Kuhn, P.; Antonietti, M.; Thomas, A. Porous, Covalent Triazine-Based Frameworks Prepared by Ionothermal Synthesis. *Angew. Chem. Int. Ed. Engl.* **2008**, *47* (18), 3450–3453.
- (58) Li, X.; Zhang, J.; Shen, L.; Ma, Y.; Lei, W.; Cui, Q.; Zou, G. Preparation and Characterization of Graphitic Carbon Nitride through Pyrolysis of Melamine. *Appl. Phys. A* **2009**, *94* (2), 387–392.

- (59) Cui, Y.; Ding, Z.; Liu, P.; Antonietti, M.; Fu, X.; Wang, X. Metal-Free Activation of H₂O₂ by g-C₃N₄ under Visible Light Irradiation for the Degradation of Organic Pollutants. *Phys. Chem. Chem. Phys.* **2012**, *14* (4), 1455–1462.
- (60) Zeng, Z.; Li, K.; Yan, L.; Dai, Y.; Guo, H.; Huo, M.; Guo, Y. Fabrication of Carbon Nitride Nanotubes by a Simple Water-Induced Morphological Transformation Process and Their Efficient Visible-Light Photocatalytic Activity. *RSC Adv.* **2014**, *4* (103), 59513–59518.
- (61) Zhu, Y.; Marianov, A.; Xu, H.; Lang, C.; Jiang, Y. Bimetallic Ag–Cu Supported on Graphitic Carbon Nitride Nanotubes for Improved Visible-Light Photocatalytic Hydrogen Production. *ACS Appl. Mater. Interfaces* **2018**, *10* (11), 9468–9477.
- (62) Chen, J.; Shen, S.; Guo, P.; Wang, M.; Su, J.; Zhao, D.; Guo, L. Plasmonic Ag@SiO₂ Core/Shell Structure Modified g-C₃N₄ with Enhanced Visible Light Photocatalytic Activity. *J. Mater. Res.* **2014**, *29* (1), 64–70.
- (63) Wang, Y.; Wang, Y.; Chen, Y.; Yin, C.; Zuo, Y.; Cui, L.-F. Synthesis of Ti-Doped Graphitic Carbon Nitride with Improved Photocatalytic Activity under Visible Light. *Mater. Lett.* **2015**, *139*, 70–72.
- (64) Guo, S.; Zhu, Y.; Yan, Y.; Min, Y.; Fan, J.; Xu, Q. Holey Structured Graphitic Carbon Nitride Thin Sheets with Edge Oxygen Doping via Photo-Fenton Reaction with Enhanced Photocatalytic Activity. *Appl. Catal. B Environ.* **2016**, *185*, 315–321.
- (65) Li, K.; Su, F.-Y.; Zhang, W.-D. Modification of G-C₃N₄ Nanosheets by Carbon Quantum Dots for Highly Efficient Photocatalytic Generation of Hydrogen. *Appl. Surf. Sci.* **2016**, *375*, 110–117.
- (66) Tian, J.; Liu, Q.; Asiri, A. M.; Sun, X.; He, Y. Ultrathin Graphitic C₃N₄ Nanofibers: Hydrolysis-Driven Top-down Rapid Synthesis and Application as a Novel Fluorosensor for Rapid, Sensitive, and Selective Detection of Fe³⁺. *Sensors Actuators B. Chem.* **2015**, *216* (Complete), 453–460.
- (67) Liu, Y.; Su, F.-Y.; Yu, Y.-X.; Zhang, W.-D. Nano G-C₃N₄ Modified Ti-Fe₂O₃ Vertically Arrays for Efficient Photoelectrochemical Generation of Hydrogen under Visible Light. *Int. J. Hydrogen Energy* **2016**, *41* (18), 7270–7279.
- (68) Fröschl, T.; Hörmann, U.; Kubiak, P.; Kučerová, G.; Pfanzelt, M.; Weiss, C. K.; Behm, R. J.; Hüsing, N.; Kaiser, U.; Landfester, K.; et al. High Surface Area Crystalline Titanium Dioxide: Potential and Limits in Electrochemical Energy Storage and Catalysis. *Chem. Soc. Rev.* **2012**, *41* (15), 5313–5360.
- (69) Zheng, Y.; Liu, J.; Liang, J.; Jaroniec, M.; Qiao, S. Z. Graphitic Carbon Nitride Materials: Controllable Synthesis and Applications in Fuel Cells and Photocatalysis. *Energy Environ. Sci.* **2012**, *5* (5), 6717–6731.
- (70) Wang, Y.; Jiang, Q.; Shang, J.; Xu, J.; Li, Y. Advances in the Synthesis of Mesoporous Carbon Nitride Materials. *Wuli Huaxue Xuebao* **2016**, *32* (8), 1913–1928.
- (71) Luo, L.; Zhang, A.; Janik, M. J.; Li, K.; Song, C.; Guo, X. Applied Surface Science Facile

- Fabrication of Ordered Mesoporous Graphitic Carbon Nitride for RhB Photocatalytic Degradation. *Appl. Surf. Sci.* **2017**, *396*, 78–84.
- (72) Park, D.; Lakhi, K. S.; Ramadass, K.; Kim, M. Energy Efficient Synthesis of Ordered Mesoporous Carbon Nitrides with a High Nitrogen Content and Enhanced CO₂ Capture Capacity. **2017**, *23955*, 10753–10757.
- (73) Long, B.; Zheng, Y.; Lin, L.; Alamry, K. A.; Asiri, A. M.; Wang, X. Cubic Mesoporous Carbon Nitride Polymers with Large Cage-Type Pores for Visible Light. *J. Mater. Chem. A Mater. energy Sustain.* **2017**, *5*, 16179–16188.
- (74) Talapaneni, S. N.; Mane, G. P.; Mano, A.; Anand, C. Synthesis of Nitrogen-Rich Mesoporous Carbon Nitride with Tunable Pores, Band Gaps and Nitrogen Content from a Single Aminoguanidine Precursor. **2012**, 700–708.
- (75) Talapaneni, S. N.; Anandan, S.; Mane, G. P.; Anand, C.; Dhawale, D. S.; Varghese, S.; Mano, A.; Mori, T.; Vinu, A. Facile Synthesis and Basic Catalytic Application of 3D Mesoporous Carbon Nitride with a Controllable Bimodal Distribution. *J. Mater. Chem.* **2012**, *22* (19), 9831–9840.
- (76) Tian, C.; Lu, C.; Wang, B.; Xie, X.; Miao, Y.; Li, X. Mesoporous Carbon Nitride as a Basic Catalyst in Dehydrochlorination of 1,1,2-Trichloroethane into 1,1-Dichloroethene. *RSC Adv.* **2015**, *5* (126), 103829–103833.
- (77) Lakhi, K. S.; Park, D.; Joseph, S.; Talapaneni, S. N.; Ravon, U. Effect of Heat Treatment on the Nitrogen Content and Its Role on the Carbon Dioxide Adsorption Capacity of Highly Ordered Mesoporous Carbon Nitride. **2017**.
- (78) Shen, W.; Ren, L.; Zhou, H.; Zhang, S.; Fan, W. Facile One-Pot Synthesis of Bimodal Mesoporous Carbon Nitride and Its Function as a Lipase Immobilization Support. *J. Mater. Chem.* **2011**, *21* (11), 3890–3894.
- (79) Yan, H. Soft-Templating Synthesis of Mesoporous Graphitic Carbon Nitride with Enhanced Photocatalytic H₂ Evolution under Visible Light. *Chem. Commun.* **2012**, *48* (28), 3430–3432.
- (80) Dai, B.; Li, X.; Zhang, J.; Yu, F.; Zhu, M. Application of Mesoporous Carbon Nitride as a Support for an Au Catalyst for Acetylene Hydrochlorination. *Chem. Eng. Sci.* **2014**, *135*, 472–478.
- (81) Datta, K. K. R.; Reddy, B. V. S.; Ariga, K.; Vinu, A. Gold Nanoparticles Embedded in a Mesoporous Carbon Nitride Stabilizer for Highly Efficient Three-Component Coupling Reaction. *Angew. Chemie Int. Ed.* **2010**, *49* (34), 5961–5965.
- (82) Elavarasan, S.; Baskar, B.; Senthil, C.; Bhanja, P.; Bhaumik, A.; Selvam, P.; Sasidharan, M. An Efficient Mesoporous Carbon Nitride (g-C₃N₄) Functionalized Pd Catalyst for Carbon-Carbon Bond Formation Reactions. *RSC Adv.* **2016**, *6* (55), 49376–49386.
- (83) Wang, Y.; Yao, J.; Li, H.; Su, D.; Antonietti, M. Highly Selective Hydrogenation of Phenol and Derivatives over a Pd@carbon Nitride Catalyst in Aqueous Media. *J. Am. Chem. Soc.* **2011**, *133* (8), 2362–2365.

- (84) Wang, F. F.; Shao, S.; Liu, C. L.; Xu, C. L.; Yang, R. Z.; Dong, W. S. Selective Oxidation of Glycerol over Pt Supported on Mesoporous Carbon Nitride in Base-Free Aqueous Solution. *Chem. Eng. J.* **2015**, *264*, 336–343.
- (85) Bello, M.; Zaidi, S. M. J.; Al-Ahmed, A.; Basu, S.; Park, D. H.; Lakhi, K. S.; Vinu, A. Pt-Ru Nanoparticles Functionalized Mesoporous Carbon Nitride with Tunable Pore Diameters for DMFC Applications. *Microporous Mesoporous Mater.* **2017**, *252*, 50–58.
- (86) Le, S.; Jiang, T.; Zhao, Q.; Liu, X.; Li, Y.; Fang, B.; Gong, M. Cu-Doped Mesoporous Graphitic Carbon Nitride for Enhanced Visible-Light Driven Photocatalysis. *RSC Adv.* **2016**, *6* (45), 38811–38819.
- (87) Qiu, P.; Chen, H.; Jiang, F. Cobalt Modified Mesoporous Graphitic Carbon Nitride with Enhanced Visible-Light Photocatalytic Activity. *RSC Adv.* **2014**, *4* (75), 39969–39977.
- (88) Guo, Y.; Liu, Q.; Li, Z.; Zhang, Z.; Fang, X. Enhanced Photocatalytic Hydrogen Evolution Performance of Mesoporous Graphitic Carbon Nitride Co-Doped with Potassium and Iodine. *Appl. Catal. B Environ.* **2018**, *221*, 362–370.
- (89) Liang, Q.; Jin, J.; Zhang, M.; Liu, C.; Xu, S.; Yao, C.; Li, Z. Construction of Mesoporous Carbon Nitride/Binary Metal Sulfide Heterojunction Photocatalysts for Enhanced Degradation of Pollution under Visible Light. *Appl. Catal. B Environ.* **2017**, *218*, 545–554.
- (90) Wang, Y.; Zhang, J.; Wang, X.; Antonietti, M.; Li, H. Boron- and Fluorine-Containing Mesoporous Carbon Nitride Poly- Mers : Metal-Free Catalysts for Cyclohexane Oxidation **. **2010**, No. 20806065.
- (91) Thind, S. S.; Mustapic, C. C.; Wen, J.; Goodwin, C. D.; Chen, A. Facile Synthesis of Mesoporous Carbon Nitride and Titanium Dioxide Nanocomposites with Enhanced Visible Light Photocatalytic Activity. *New J. Chem.* **2017**, *41* (19), 10542–10549.
- (92) Chem, J. M. Mesoporous Carbon Nitride with in Situ Sulfur Doping for Enhanced Photocatalytic Hydrogen Evolution from Water under Visible Light. **2012**, 15006–15012.
- (93) Kailasam, K.; Fischer, A.; Zhang, G.; Zhang, J.; Thomas, A. Mesoporous Carbon Nitride-Tungsten Oxide Composites for Enhanced Photocatalytic Hydrogen Evolution. **2015**, 1404–1410.
- (94) Xu, J.; Jiang, Q.; Chen, T.; Wu, F.; Li, Y.-X. Vanadia Supported on Mesoporous Carbon Nitride as a Highly Efficient Catalyst for Hydroxylation of Benzene to Phenol. *Catal. Sci. Technol.* **2015**, *5* (3), 1504–1513.
- (95) Luo, L.; Zhang, A.; Janik, M. J.; Song, C.; Guo, X. Mesoporous Graphitic Carbon Nitride Functionalized Iron Oxides for Promoting Phenol Oxidation Activity. *RSC Adv.* **2016**, *6* (94), 91960–91967.
- (96) Yang, S.; Zhou, W.; Ge, C.; Liu, X.; Fang, Y.; Li, Z. Mesoporous Polymeric Semiconductor Materials of Graphitic-C₃N₄: General and Efficient Synthesis and Their Integration with Synergistic AgBr NPs for Enhanced Photocatalytic Performances. *RSC Adv.* **2013**, *3* (16), 5631.

- (97) Lin, Z.; Wang, X. Nanostructure Engineering and Doping of Conjugated Carbon Nitride Semiconductors for Hydrogen Photosynthesis. *Angew. Chemie - Int. Ed.* **2013**, *52* (6), 1735–1738.
- (98) Xue, X. Y.; Yuan, S.; Xing, L. L.; Chen, Z. H.; He, B.; Chen, Y. J. Porous Co₃O₄ nanoneedle Arrays Growing Directly on Copper Foils and Their Ultrafast Charging/Discharging as Lithium-Ion Battery Anodes. *Chem. Commun.* **2011**, *47* (16), 4718–4720.
- (99) Sun, L. B.; Yang, J.; Kou, J. H.; Gu, F. N.; Chun, Y.; Wang, Y.; Zhu, J. H.; Zou, Z. G. One-Pot Synthesis of Potassium-Functionalized Mesoporous γ -Alumina: A Solid Superbase. *Angew. Chemie - Int. Ed.* **2008**, *47* (18), 3418–3421.
- (100) Gao, X.; Jiao, X.; Zhang, L.; Zhu, W.; Xu, X.; Ma, H.; Chen, T. Cosolvent-Free Nanocasting Synthesis of Ordered Mesoporous g-C₃N₄ and Its Remarkable Photocatalytic Activity for Methyl Orange Degradation. *RSC Adv.* **2015**, *5* (94), 76963–76972.
- (101) Deng, Q. F.; Liu, L.; Lin, X. Z.; Du, G.; Liu, Y.; Yuan, Z. Y. Synthesis and CO₂ capture Properties of Mesoporous Carbon Nitride Materials. *Chem. Eng. J.* **2012**, *203*, 63–70.
- (102) Xu, H.; Hai, Z.; Diwu, J.; Zhang, Q.; Gao, L.; Cui, D.; Zang, J.; Liu, J.; Xue, C. Synthesis and Microwave Absorption Properties of Core-Shell Structured Co₃O₄-PANI Nanocomposites. *J. Nanomater.* **2015**, *2015*, 1–8.
- (103) He, T.; Chen, D.; Jiao, X.; Xu, Y.; Gu, Y. Surfactant-Assisted Solvothermal Synthesis of Co₃O₄ Hollow Spheres with Oriented-Aggregation Nanostructures and Tunable Particle Size. *Langmuir* **2004**, *20* (19), 8404–8408.
- (104) Xu, J.; Wu, H.-T.; Wang, X.; Xue, B.; Li, Y.-X.; Cao, Y. A New and Environmentally Benign Precursor for the Synthesis of Mesoporous G-C₃N₄ with Tunable Surface Area. *Phys. Chem. Chem. Phys.* **2013**, *15* (13), 4510.
- (105) Ye, L.; Liu, J.; Gong, C.; Tian, L.; Peng, T.; Zan, L. Two Different Roles of Metallic Ag on Ag/AgX/BiOX (X = Cl, Br) Visible Light Photocatalysts: Surface Plasmon Resonance and Z-Scheme Bridge. *ACS Catal.* **2012**, *2* (8), 1677–1683.
- (106) Chen, P. W.; Li, K.; Yu, Y. X.; Zhang, W. De. Cobalt-Doped Graphitic Carbon Nitride Photocatalysts with High Activity for Hydrogen Evolution. *Appl. Surf. Sci.* **2017**, *392*, 608–615.
- (107) Zhu, X.; Wang, J.; Nguyen, D.; Thomas, J.; Norwood, R. A.; Peyghambarian, N. Linear and Nonlinear Optical Properties of Co₃O₄ Nanoparticle-Doped Polyvinyl-Alcohol Thin Films. *Opt. Mater. Express* **2012**, *2* (1), 103.
- (108) Robertson, J.; O'Reilly, E. P. Electronic and Atomic Structure of Amorphous Carbon. *Phys. Rev. B* **1987**, *35* (6), 2946–2957.
- (109) Silva, S. R. P.; Robertson, J.; Amaratunga, G. A. J.; Rafferty, B.; Brown, L. M.; Schwan, J.; Franceschini, D. F.; Mariotto, G. Nitrogen Modification of Hydrogenated Amorphous Carbon Films. *J. Appl. Phys.* **1997**, *81* (6), 2626–2634.

References

- (110) Wang, Q.; Lian, J.; Li, J.; Wang, R.; Huang, H.; Su, B.; Lei, Z. Highly Efficient Photocatalytic Hydrogen Production of Flower-like Cadmium Sulfide Decorated by Histidine. *Sci. Rep.* **2015**, *5*, 13593.
- (111) Li, T.; Zhao, L.; He, Y.; Cai, J.; Luo, M.; Lin, J. Synthesis of G-C₃N₄/SmVO₄ Composite Photocatalyst with Improved Visible Light Photocatalytic Activities in RhB Degradation. *Appl. Catal. B Environ.* **2013**, *129*, 255–263.
- (112) Shi, H.; Chen, G.; Zhang, C.; Zou, Z. Polymeric G-C₃N₄ Coupled with NaNbO₃ Nanowires toward Enhanced Photocatalytic Reduction of CO₂ into Renewable Fuel. *ACS Catal.* **2014**, *4* (10), 3637–3643.
- (113) Xiong, Z.; Lei, Z.; Kuang, C.-C.; Chen, X.; Gong, B.; Zhao, Y.; Zhang, J.; Zheng, C.; Wu, J. C. S. Selective Photocatalytic Reduction of CO₂ into CH₄ over Pt-Cu₂O/TiO₂ Nanocrystals: The Interaction between Pt and Cu₂O Cocatalysts. *Appl. Catal. B Environ.* **2017**, *202*, 695–703.
- (114) Liu, Y.; Lv, Y.; Zhu, Y.; Liu, D.; Zong, R.; Zhu, Y. Fluorine Mediated Photocatalytic Activity of BiPO₄. *Appl. Catal. B Environ.* **2014**, *147*, 851–857.
- (115) McShane, C. M.; Choi, K.-S. Photocurrent Enhancement of N-Type Cu₂O Electrodes Achieved by Controlling Dendritic Branching Growth. *J. Am. Chem. Soc.* **2009**, *131* (7), 2561–2569.
- (116) Yu, L.; Zhang, X.; Li, G.; Cao, Y.; Shao, Y.; Li, D. Highly Efficient Bi₂O₂CO₃/BiOCl Photocatalyst Based on Heterojunction with Enhanced Dye-Sensitization under Visible Light. *Appl. Catal. B Environ.* **2016**, *187*, 301–309.
- (117) Thaweesak, S.; Wang, S.; Lyu, M.; Xiao, M.; Peerakiatkhajohn, P.; Wang, L. Boron-Doped Graphitic Carbon Nitride Nanosheets for Enhanced Visible Light Photocatalytic Water Splitting. **2017**, 10714–10720.
- (118) Yu, J.; Ma, T.; Liu, S. Enhanced Photocatalytic Activity of Mesoporous TiO₂ Aggregates by Embedding Carbon Nanotubes as Electron-Transfer Channel. *Phys. Chem. Chem. Phys.* **2011**, *13* (8), 3491–3501.
- (119) Kim, Y. I.; Atherton, S. J.; Brigham, E. S.; Mallouk, T. E. Sensitized Layered Metal Oxide Semiconductor Particles for Photochemical Hydrogen Evolution from Nonsacrificial Electron Donors. *J. Phys. Chem.* **1993**, *97* (45), 11802–11810.
- (120) Butler, M. A. Prediction of Flatband Potentials at Semiconductor-Electrolyte Interfaces from Atomic Electronegativities. *J. Electrochem. Soc.* **1978**, *125* (2), 228.
- (121) Xu, Y.; Schoonen, M. A. A. The Absolute Energy Positions of Conduction and Valence Bands of Selected Semiconducting Minerals. *Am. Mineral.* **2000**, *85* (3–4), 543–556.
- (122) Tang, J.; Zou, Z.; Ye, J. Photophysical and Photocatalytic Properties of AgInW₂O₈. *J. Phys. Chem. B* **2003**, *107* (51), 14265–14269.
- (123) Kudo, A.; Omori, K.; Kato, H. A Novel Aqueous Process for Preparation of Crystal Form-

- Controlled and Highly Crystalline BiVO₄ Powder from Layered Vanadates at Room Temperature and Its Photocatalytic and Photophysical Properties. *J. Am. Chem. Soc.* **1999**, *121* (49), 11459–11467.
- (124) Suyana, P.; Ganguly, P.; Nair, B. N.; Mohamed, A. P.; Warriar, K. G. K.; Hareesh, U. S. Co₃O₄-C₃N₄p-n Nano-Heterojunctions for the Simultaneous Degradation of a Mixture of Pollutants under Solar Irradiation. *Environ. Sci. Nano* **2017**, *4* (1), 212–221.
- (125) Chang, X.; Wang, T.; Zhang, P.; Zhang, J.; Li, A.; Gong, J. Enhanced Surface Reaction Kinetics and Charge Separation of P–n Heterojunction Co₃O₄/BiVO₄ Photoanodes. *J. Am. Chem. Soc.* **2015**, *137* (26), 8356–8359.
- (126) Suyana, P.; K. R., S.; Nair, B. N.; Karunakaran, V.; Mohamed, A. P.; Warriar, K. G. K.; Hareesh, U. S. A Facile One Pot Synthetic Approach for C₃N₄–ZnS Composite Interfaces as Heterojunctions for Sunlight-Induced Multifunctional Photocatalytic Applications. *RSC Adv.* **2016**, *6* (22), 17800–17809.
- (127) Dai, K.; Li, D.; Lu, L.; Liu, Q.; Liang, C.; Lv, J.; Zhu, G. Plasmonic TiO₂/AgBr/Ag Ternary Composite Nanosphere with Heterojunction Structure for Advanced Visible Light Photocatalyst. *Appl. Surf. Sci.* **2014**, *314*, 864–871.
- (128) Chen, L.-Y.; Zhang, W.-D. In₂O₃/g-C₃N₄ Composite Photocatalysts with Enhanced Visible Light Driven Activity. *Appl. Surf. Sci.* **2014**, *301*, 428–435.